University of Tartu
Faculty of Science and Technology
Institute of Physics

Robert Aare

Two temperature model simulations of femtosecond-laser-induced faceting on tungsten surfaces

Master's thesis

Supervisor: PhD Vahur Zadin

Tartu 2018

Title

Two temperature model simulations of femtosecond-laser-induced faceting on tungsten surfaces

Author

Robert Aare

Abstract

The CLIC linear particle collider, which is currently under design at CERN, uses extremely high electric fields for particle acceleration. The practicable acceleration gradient is limited by the occurrence of spontaneous vacuum breakdowns, which are hypothesized to be governed by electric field driven surface changes. A recent experiment by H. Yanagisawa *et al.* revealed reproducible gradual facet formation and possible nanotip growth on a microscopically sharp femtosecond-laser-irradiated tungsten tip surface. Understanding the mechanism leading to surface modifications due to interaction with electromagnetic waves may help discover the process leading to vacuum breakdowns in accelerators as well as enhance experimental techniques like electron holography and electron microscopy.

In this thesis, a comprehensive computational model for describing ultrafast thermal, mechanical and electrical effects in a tungsten tip is assembled, centered on the two temperature model. It is shown that, although the temperature of the atomic lattice in the tungsten tip does not reach the melting temperature of tungsten, the thermal stresses are sufficient for plastic deformations to occur in a significant portion of the tip. This result is complemented with multiscale simulations of emission patterns on atomistic surfaces, that show an electrostatic field driven surface diffusion process, which leads to the merging of neighbouring field emission sites, ultimately leading to the emergence of a dominant emitter. The findings are used for formulating a proposed mechanism that explains the observations made by H. Yanagisawa *et al.* in the experiment.

Keywords

Two temperature model, femtosecond laser, surface modification, emission currents, multiscale simulations

CERCS code

P250 (Condensed matter: structure, thermal and mechanical properties, crystallography, phase equilibria)

Pealkiri

Volframi pinnadefektide tekke modelleerimine femtosekundlaserieksperimentides

Autor

Robert Aare

Lühikokkuvõte

Kompaktne lineaarpõrguti (CLIC), mida hetkel Euroopa Tuumauuringute Keskuses (CERN) projekteeritakse, kasutab osakeste kiirendamiseks elektrivälju, mille tugevuse üheks piiravaks faktoriks on spontaansete vaakumläbilöökide esinemine. Läbilöökide arvatavaks põhjuseks on elektriväljast tingitud defektide teke kiirendikomponentide pindadel. H. Yanagisawa jt. hiljutises eksperimendis avastati, et mikroskoopilise volframtipu kestval femtosekundiliste laseriimpulssidega kiiritamisel omandab tipu kiiritatud osa hulktahukalise profiili, millele aegamisi tekib nanoskoopiline teravik. Pinnamuutusteni viivate mehhanismide mõistmine võib viia vaakumläbilöökide tekkeprotsessi avastamiseni, aga ka nanoskoopilisi tippe elektronide allikana kasutavate eksperimentaalsete meetodite, näiteks elektronmikroskoopia täiustamiseni.

Käesolevas töös koostati kahe temperatuuri mudelil põhinev arvutusmudel, mis simuleerib ülikiireid termilisi, mehhaanilisi ning elektrilisi efekte volframtipus, millega näidati, et ehkki laseri energia neeldumine ei vii sulamistemperatuuri jõudmiseni volframtipu kristallvõres, esineb tipus märkimisväärsel määral soojuspaisumisest tingitud plastilisi deformatsioone. Selle tulemuse täiendamiseks koostati multimastaapne simulatsioon, mis keskendub elektronide emissioonile elektrostaatilises väljas olevatelt atomistlikelt pindadelt. Multimastaapse simulatsiooni tulemustest selgus mehhanism, mille mõjul üksteise naabruses olevad emitterid ühinevad elektrivälja poolt mõjutatud pinnadifusiooni tõttu, põhjustades seega lokaalselt domineeriva emitteri tekke. Leitud tulemustest formuleeriti võimalik mehhanism H. Yanagisawa jt. eksperimendis moodustunud pinnavormide tekkeks.

Võtmesõnad

Kahe temperatuuri mudel, femtosekundlaser, pinnadefektid, emissioonivoolud, multimastaapsed simulatsioonid

CERCS kood

P250 (Tahke aine: struktuur, termilised ja mehhaanilised omadused, kristallograafia, *phase equilibria*)

Table of contents

1 Introduction

1.1 Background

The Compact Linear Collider (CLIC) is a particle accelerator, that is currently under design at the European Organization for Nuclear Research (CERN), and aims to achieve electron-positron collisions at energies of up to 3 TeV. In order to reach the desired collision energies, the particles are accelerated with an electric field of 100 MV/m, at the frequency of 12 GHz. The use of accelerating electric fields of that magnitude, however, leads to vacuum breakdowns on the surfaces of the accelerating structure, resulting in significant damage to the accelerator components, and losses in the accelerated particle beams. Thus, breakdowns are a limiting factor for practicable accelerating fields, which, in addition to particle accelerators in science experiments, can also affect the design constraints of radiotherapy devices [1-6].

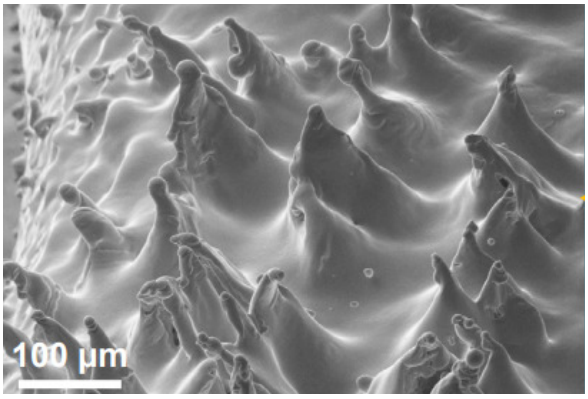

Illustration 1:

Structures grown on an accelerator component surface during high-field tests [7].

The reason for vacuum breakdowns is thus far unknown. It is hypothesized, that the spontaneous breakdowns occurring on the CLIC accelerator components are governed by high electric field driven surface modifications, an example of which is shown in **illustration 1** [2].

In a recent experiment by H. Yanagisawa *et al.*, irradiating a microscopic tungsten tip with repeated femtosecond laser impulses in the presence of a strong DC electric field revealed **gradual, reproducible surface faceting and possible nanotip growth**. The purpose of the experiment was to fabricate nanotips, using laser impulses, in order to exploit the formed metal nanotips as sources of pulsed bright and coherent electron waves during laser impulse irradiation [9-11]. Forming a nanotip on a larger tip during the experiment by the laser itself simplifies the fabrication process compared to current well established methods, by avoiding complications related to keeping the present sensitive optical elements clean [9].

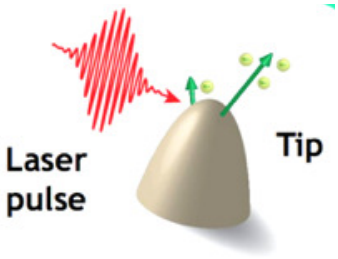

Illustration 2:

The laser impulse irradiates the tip in horizontal direction [8,9].

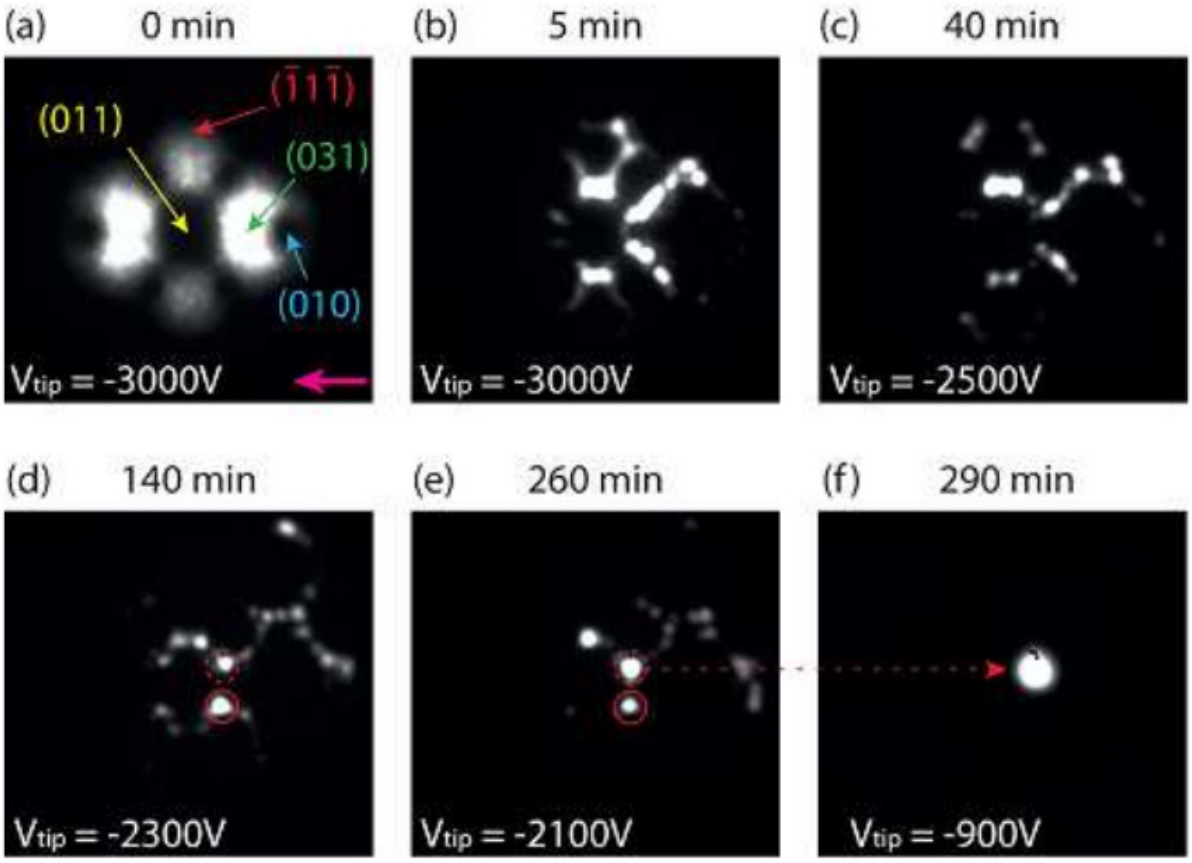

Illustration 3:

Field emission microscope images taken from the tip, depicting the change in emission pattern due to topology change over time, while accumulating laser impulse irradiation. In image (a) different crystal surfaces are shown. The pink arrow in image (a) shows laser impulse direction. Time passed since the start of the experiment is given above each frame. Voltage applied on the tip, shown on each frame, was chosen, so as to reach a certain emission current threshold [9].

Topology changes were observed *in situ*, using field emission microscopy. As shown in **illustration 3**, recorded field emission patterns are taken from directly above the tip. Smoothed by flash heating prior to the start of the irradiation, the emission pattern (see frame *(a)* in illustration 3) initially follows crystal surface orientations, owing to differences in surface work functions [12]. Due to laser irradiation, however, the emission patterns converge over time on the edges of the initial crystal surfaces, signifying facet formation.

The patterns form more emphatically on the laser-irradiated side of the tip, hinting at the effect of the laser in the process. Eventually a single emission spot remains, marking the emergence of a dominant field-emitting nanotip [9].

Scanning electron microscope images, shown in **illustration 4**, reveal several facets formed on the tip, combining into sharp edges and corners at overlap areas. The sharpness equates to a higher local

field enhancement factor, and explains the field emission pattern convergence phenomenon. Namely, field emission current density, described by the Fowler-Nordheim model, depends on the square of the local field enhancement factor [9,13].

The formation of facets on tungsten single-crystal field emitters is itself not a new phenomenon. Polyhedral shapes on surfaces have emerged in experiments, where the emitter is subjected to heating under a strong electrostatic field [14-16].

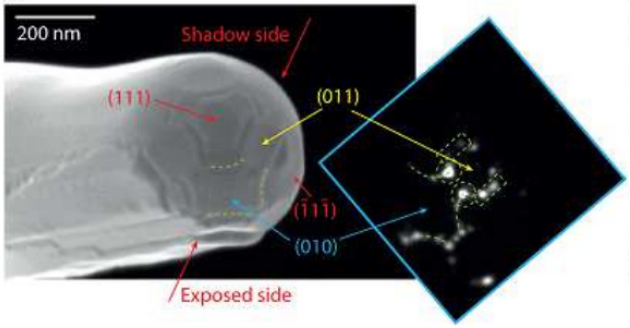

Illustration 4:

Scanning electron microscope image of a faceted tungsten tip, with the corresponding field emission pattern. The shadow side of the tip is remarkably smooth compared to the side exposed to the laser [9].

In the case of the experiment at hand, the tip was **not subjected to any direct heating**. Thus, any temperature rise in the tip had to be caused by the **energy absorbed from the laser impulses**, which itself explains the asymmetry of the topology change. In other words, the laser impulses behave as a local heat source. As the laser impulses are sub-10-fs in length, the laser pulse energy is given to the electrons, which then gradually heat up the crystal lattice of the tip. The laser operated at high optical and low infrared wavelengths, with a power of $P_{laser} = 180\,mW$, with spectrum provided in **appendix C** [9,17].

A computational model by C. Kealhofer *et al.,* developed for studying electron emission from HfC tips under similar conditions, estimated, that the lattice temperature peaks 3 ps after each laser impulse, and is distributed very asymmetrically. A distinctly higher temperature remains in the tip for a few nanoseconds, until equilibration leads to a uniform temperature distribution. Yanagisawa *et al.* estimated, that the tungsten tip reaches a maximum temperature of around **4200 K**, which would mean that the top layer of tungsten would momentarily acquire liquid properties. For a more comprehensive analysis, to verify the occurrence of such a phenomenon, a more detailed approach is necessary [9,17].

Nanoscopically sharp field emission tips are used as electron sources in experimental techniques like electron holography, coherent electric diffraction and electron microscopy, due to their charateristic high brightness, large transverse coherence length, and small energy spread. Combining field emitters with femtosecond-regime lasers enables observing physical effects in materials in the femtosecond scale with atomic spatial resolution. Advances in understanding the

material response in ultrafast timescales therefore have the potential to enhance the aforementioned experimental techniques, and help discover the elusive mechanism leading to spontaneous vacuum breakdowns on accelerator component surfaces in CLIC [9,17].

1.2 Objectives of this work

This work aims to investigate ultrafast processes, driven by laser and tungsten surface interaction, to find a possible mechanism leading to surface faceting in the experiment by H. Yanagisawa *et al*. This necessitates the creation of computational models, that enable calculating effects occurring in a tungsten crystal subjected to high electrostatic fields and laser irradiation. The steps necessary to be taken to reach the objective of this work can be expressed followingly:

- Creating a dynamical multiphysics 3D model, based on the finite element method, that enables simulating the interaction between laser impulses and the tungsten surface, taking into account the following physical effects:
  - heating effects from laser impulse energy dissipation in tungsten surface layer
  - emission currents induced by the laser impulses and the present electrostatic field
  - emission currents' dependence on crystal surface orientation
  - secondary heating effects due to emission currents
  - equilibration of electronic and lattice temperatures based on the two temperature model
- Using the model to calculate the characteristic behaviour of electronic and lattice temperatures and emission currents for a single laser impulse timeframe (*ca* 10 fs) and the following temperature equilibration time (*ca* 10 ns).
- Complementing obtained results with atomistic models describing atom migration effects on the topology under the calculated surface conditions.
- Formulating an explanation for the experimental observations, based on the analysis of the acquired results.

1.3 Author's contribution

The initial two-temperature model for describing ultrafast thermal effects in the tungsten tip, as well as an initial algorithm for surface orientation detection, was implemented by Vahur Zadin, PhD. To this model, the author added additional physical effects, geometrical modifications and refinements to the surface orientation detection algorithm. The General Thermal Field equation for modelling

tips with continuum models, along with the Nottingham effect, was created by Kristjan Eimre, and adapted to the current task by the author. The atomistic calculations presented in this work were conducted by Ekaterina Baibuz from the University of Helsinki. The Kimocs model for atomistic surface diffusion was provided by Ville Jansson, PhD, and the initial estimation for laser energy deposition in the tungsten crystal was provided by Henriqué Vázquéz, both also from the University of Helsinki.

All calculations, plots, images and text presented in this work were created by the author, apart from illustrations 1-4, 6, 23, 25a and 27, and the atomistic simulations.

2 Theoretical overview

2.1 Interaction of the physical models in this work

A description of the physical dynamics in the tungsten tip under laser irradiation necessitates the interaction of several physical effects. The electromagnetic waves partially propagate into the tungsten crystal, dissipate, and thus heat up the electronic subsystem. The electrons interact with the atomic lattice via electron-phonon interaction. The presence of an electrostatic field due to *in situ* field emission microscopy, and possible high temperatures at the tip result in emission currents, with introduce a number of other thermal effects and mechanical stresses. The interaction mechanisms between these physical effects are compiled into a single flowchart, shown in **illustration 5**, and are described in detail further on.

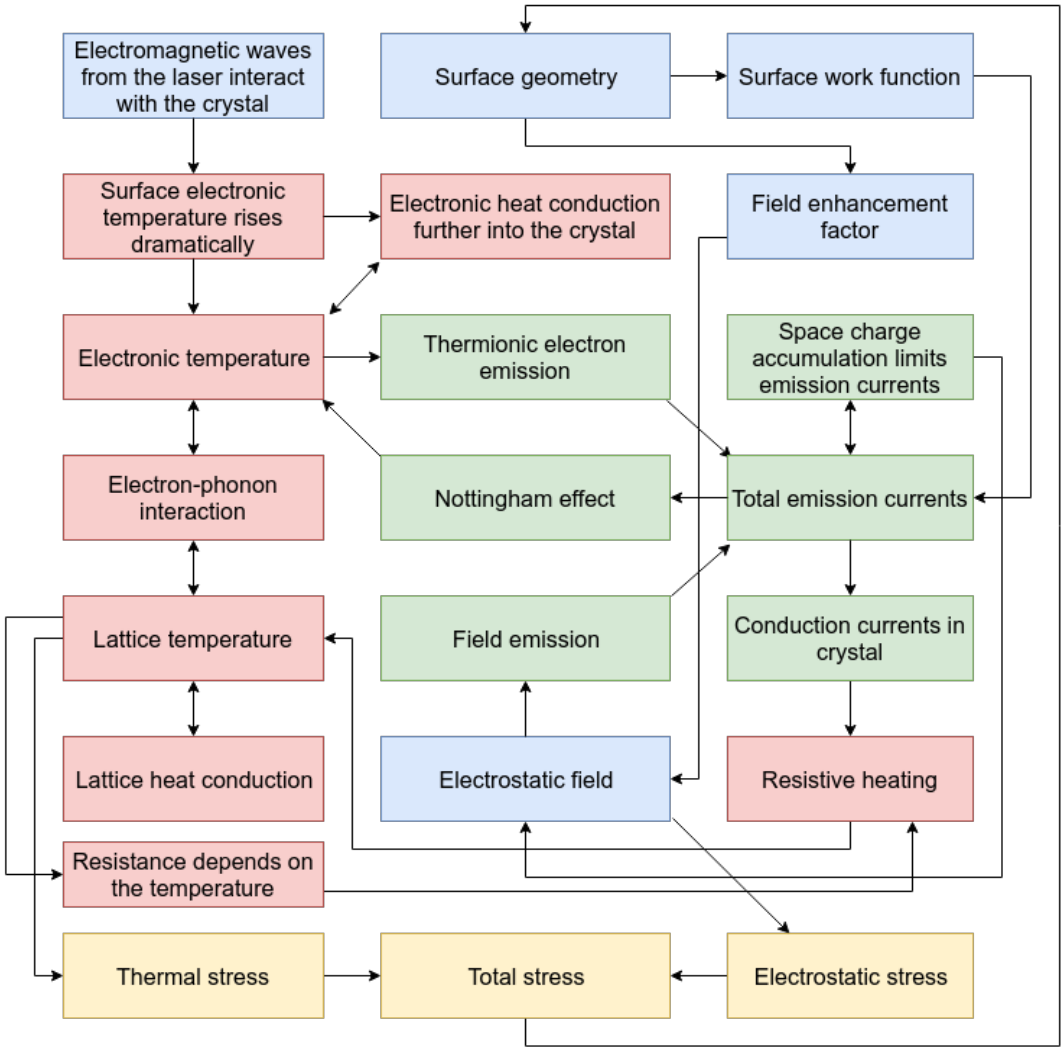

Illustration 5:

Interactions between the physical effects taken into account in the model. Experimental initial conditions are given in blue, the two temperature model and other thermal effects in red, effects related to emission currents in green and mechanical stresses in yellow.

2.2 Electromagnetic fields

2.2.1 Maxwell's equations and fundamental electromagnetic quantities

Elecromagnetic fields are described by Maxwell's equations, which describe relations between fundamental electromagnetic quantities, listed below [18-19]:

- Electric field intensity $\boldsymbol{E}(V/m)$
- Electric displacement or electric flux density $\boldsymbol{D}(C/m^2)$
- Magnetic field intensity $\boldsymbol{H}(A/m)$
- Magnetic flux density $\boldsymbol{B}(T)$
- Electrical current density $\boldsymbol{J}(A/m^2)$
- Electric charge density $\rho(C/cm^3)$

Maxwell's equations for vacuum are given in differential form, as follows:

- Ampere-Maxwell's law [18-19]:

$$\nabla \times \boldsymbol{H} = \boldsymbol{J} + \frac{\partial \boldsymbol{D}}{\partial t} \tag{1}$$

- Faraday's law [18-19]:

$$\nabla \times \boldsymbol{E} = -\frac{\partial \boldsymbol{B}}{\partial t} \tag{2}$$

- Gauss' law [18-19]:

$$\nabla \cdot \boldsymbol{D} = \rho \tag{3}$$

- Gauss' law in magnetism [18-19]:

$$\nabla \cdot \boldsymbol{B} = 0 \tag{4}$$

In materials, electromagnetic fields are somewhat more complicated to describe, due to the medium responding to the field. This necessitates the introduction of the following relations [18]:

$$\boldsymbol{D} = \epsilon_0 \boldsymbol{E} + \boldsymbol{P} \tag{5}$$

$$\boldsymbol{B} = \mu_0 (\boldsymbol{H} + \boldsymbol{M}) \tag{6}$$

Where ϵ_0 and μ_0 are vacuum permittivity and permeability, respectively [19]:

$$\epsilon_0 = 8.8542 \cdot 10^{-12} \frac{F}{m}$$
$$\mu_0 = 4\pi \cdot 10^{-7} \frac{H}{m} \quad (7)$$

The polarization vector $\boldsymbol{P}$ describes material polarization in the presence of an electric field, and can be interpreted as electric dipole moment density. In most cases, polarization depends on the applied electric field $\boldsymbol{E}$. Ferroelectric materials, however, exhibit permanent polarization without an external electric field [18,20].

Analogously, magnetization vector $\boldsymbol{M}$ describes the magnetization induced in the material by the external magnetic field, and is to be interpreted as magnetic dipole moment density. $\boldsymbol{M}$ is usually some function of $\boldsymbol{H}$. Ferromagnetics exhibit permanent magnetization without the presence of an external magnetic field [18].

In some cases, it's easier to formulate problems, using electric scalar potential V and magnetic vector potential **A**, defined through the following equations [18]:

$$\boldsymbol{B} = \nabla \times \boldsymbol{A}$$
$$\boldsymbol{E} = -\nabla V - \frac{\partial \boldsymbol{A}}{\partial t} \quad (8)$$

2.2.2 Electrostatic field

If charge carriers are present, Gauss' law (**eq. 3**) necessitates the existence of an electrostatic field. In an empty space between charge carriers, Gauss' law presents itself as the Laplace equation, the solution of which depends only on the boundary conditions [4,13]:

$$\nabla^2 V = 0 \quad (9)$$

Here V is the electrostatic potential. The electric field can be calculated from the potential distribution, as follows [21]:

$$\boldsymbol{E} = -\nabla V \quad (10)$$

In the case of flat electrodes with ideally smooth surfaces, the resulting electric field distribution would be uniform. The presence of a surface bump or some other defect enhances the local electric field, potentially increasing the electric field by up to 2 orders of magnitude near a tip, depending on the exact topology. The field enhancement factor β_E is defined as the ratio of the local electrostatic field strength at the tip, E_{tip}, and the electrostatic field strength far enough from the tip, for the electric field distribution to be approximately uniform, E_{far} [4-5,13]:

$$\beta_E = \frac{E_{tip}}{E_{far}} \tag{11}$$

2.2.3 Electromagnetic waves

Maxwell's laws predict the existence of electromagnetic waves. Assuming that there are **no charges present**, the Maxwell equations can be used to derive the Helmholtz wave equation (see appendix A), which is identical in form for both the electric and magnetic waves [19,22-24]:

$$\begin{aligned} \frac{1}{\mu_0 \epsilon_0} \nabla^2 \boldsymbol{E} &= \frac{\partial^2 \boldsymbol{E}}{\partial t^2} \\ \frac{1}{\mu_0 \epsilon_0} \nabla^2 \boldsymbol{B} &= \frac{\partial^2 \boldsymbol{B}}{\partial t^2} \end{aligned} \tag{12}$$

The Helmholtz wave equations for the electric and magnetic fields are satisfied by the following general waveform solutions [19,22-24]:

$$\begin{aligned} \boldsymbol{E} &= \boldsymbol{E_0} e^{i(\boldsymbol{k}\cdot\boldsymbol{r} - \omega t)} \\ \boldsymbol{B} &= \boldsymbol{B_0} e^{i(\boldsymbol{k}\cdot\boldsymbol{r} - \omega t)} \end{aligned} \tag{13}$$

Here $\boldsymbol{E_0}; \boldsymbol{B_0}$ are the amplitude values for electric and magnetic fields, respectively, ω is the angular frequency of the electromagnetic wave, $\boldsymbol{r}$ is the location vector, and $\boldsymbol{k}$ is the wave vector. Maxwell's laws require the waveform solutions for electric and magnetic fields to be dependent on one another. The waves propagate with the square root of the constant in the Helmholtz wave equation, which in the vacuum environment is the speed of light [19,22]:

$$c = \frac{1}{\sqrt{\mu_0 \epsilon_0}} \tag{14}$$

2.2.4 The dynamics of electromagnetic waves in materials

Electromagnetic waves dynamically affect the surrounding charge carriers. Depending on the material the wave propagates in as well as the wave properties, the material can significantly affect the wave in return. The behaviour of an electromagnetic wave of some frequency ω is therefore determined by the environment response to the respective wave. Assuming an **isotropic medium**, the polarization $\boldsymbol{P}$ of the environment, defined earlier, is written in the following form [25-27]:

$$\boldsymbol{P}(\boldsymbol{r}, t) = \epsilon_0 \chi_e(\omega) \boldsymbol{E}(\boldsymbol{r}, t) \tag{15}$$

Here $\chi_e(\omega)$ is the electrical susceptibility of the material. The electrical permittivity of the medium, $\epsilon(\omega)$, is then written as follows [26]:

$$\epsilon(\omega) = 1 + \chi_e(\omega) \tag{16}$$

The frequency-dependent electrical permittivity of a medium, is generally a complex number, describing the material's response to electromagnetic waves averaged over many atoms [26,28]:

$$\begin{gathered}\epsilon(\omega)=\epsilon_1(\omega)+i\epsilon_2(\omega)\\ \Re(\epsilon(\omega))=\epsilon_1(\omega)\\ \Im(\epsilon(\omega))=\epsilon_2(\omega)\end{gathered} \tag{17}$$

Metals generally have a very high imaginary part of the complex permittivity, as well as a negative real part, at low frequencies [28-29]. A first approximation for estimating the real part of the complex electrical permittivity can be made according to the Drude theory of metals as follows [27]:

$$\Re\epsilon(\omega)=1-\frac{\omega_p^2}{\omega^2} \tag{18}$$

Here, ω_p is plasma frequency, with n_e marking electron number density, m_e marking effective electron mass, and e_0 is the charge of an electron [27]:

$$\omega_p=\sqrt{\frac{4\pi n_e e_0^2}{m_e}} \tag{19}$$

At low frequencies, where the real part of the complex permittivity is negative, radiation cannot propagate in the metal [27]. At high frequencies, where the real part of complex permittivity becomes positive, electromagnetic waves can propagate in the metal, whereupon the imaginary part of the complex permittivity will determine the loss factor, as shown later on. At frequencies higher than plasma frequency, metals become transparent [27-29].

In electrical conductors, electrical current density is determined by the frequency-dependent complex conductivity $\sigma(\omega)$ and the incident electric field [18,25-27,29]:

$$\boldsymbol{J}=\sigma(\omega)\boldsymbol{E} \tag{20}$$

It is possible to formulate Maxwell's laws in such a way that a generalized complex permittivity contains complex conductivity, which can be useful, when dealing with high-frequency electromagnetic fields. In that formalism, Ampere-Maxwell's law (eq. 1) is in the following form (derivation given in appendix B) [26]:

$$\nabla\times\boldsymbol{H}=\frac{\partial\boldsymbol{D}}{\partial t} \tag{21}$$

And Gauss' law (eq. 3) transforms into (see appendix B) [26]:

$$\nabla\cdot\boldsymbol{E}=0 \tag{22}$$

The magnetic flux density and field intensity are related in an isotropic material as follows [25]:

$$\boldsymbol{B}=\mu_0\mu_m(\omega)\boldsymbol{H} \tag{23}$$

Here, $\mu_m(\omega)$ is magnetic permeability. Magnetic susceptibility $\chi_m(\omega)$ is then [25-26]:

$$\mu_m(\omega)=\chi_m(\omega)+1 \tag{24}$$

Similarly to electrical permittivity, magnetic permeability is also generally a complex number, dependent on the frequency of the electromagnetic wave [26,29-30]:

$$\begin{gathered}\mu(\omega)=\mu_1(\omega)+i\mu_2(\omega)\\ \Re(\mu(\omega))=\mu_1(\omega)\\ \Im(\mu(\omega))=\mu_2(\omega)\end{gathered} \tag{25}$$

Complex magnetic permeability has mathematical properties similar to those of the complex electrical permittivity. At already relatively low frequencies, however, magnetic susceptibility loses any physical meaning. Magnetic permeability can therefore be set to unity at even below optical frequencies [29].

The complex electrical permittivity and magnetic permeability determine the macroscopic optical constants of the material. Assuming, that the incident wave is a homogeneous plane wave, the index of refraction, that determines the phase velocity of the electromagnetic wave in the medium, can be calculated with the following formula [25-26,29]:

$$n(\omega)=\sqrt{\frac{\epsilon_1(\omega)\mu_1(\omega)-\epsilon_2(\omega)\mu_2(\omega)+\sqrt{(\epsilon_1(\omega)^2+\epsilon_2(\omega)^2)(\mu_1(\omega)^2+\mu_2(\omega)^2)}}{2}} \tag{26}$$

The loss factor, that determines the rate of wave energy dissipation, as the wave propagates in the medium, can be calculated, as follows [26]:

$$\kappa(\omega)=\sqrt{\frac{-\epsilon_1(\omega)\mu_1(\omega)+\epsilon_2(\omega)\mu_2(\omega)+\sqrt{(\epsilon_1(\omega)^2+\epsilon_2(\omega)^2)(\mu_1(\omega)^2+\mu_2(\omega)^2)}}{2}} \tag{27}$$

Calculation of the refraction index and loss factor simplify greatly, if the complex magnetic permeability is 1. The index of refraction and loss factor, in turn, determine the reflectivity R [26]:

$$R(\omega)=\frac{(n(\omega)-1)^2+\kappa(\omega)^2}{(n(\omega)+1)^2+\kappa(\omega)^2} \tag{28}$$

2.2.5 Dissipation of the energy of an electromagnetic wave

The energy flux density $\boldsymbol{S}$ of an electromagnetic wave is defined through the Poynting vector [26,29]:

$$\boldsymbol{S}=\boldsymbol{E}\times\boldsymbol{H} \tag{29}$$

The rate of energy change in the volume the electromagnetic wave travels in can be calculated straightforwardly, as the divergence of the wave energy flux. Using Maxwell's laws in the generalized form (eq. 2, 4, 21-22), the following result is reached [26,29]:

$$-\nabla \cdot \boldsymbol{S} = \boldsymbol{E}\frac{\partial \boldsymbol{D}}{\partial t} + \boldsymbol{H}\frac{\partial \boldsymbol{B}}{\partial t} \tag{30}$$

By keeping only the real values of the electromagnetic wave vector components and averaging over one wave oscillation period, the following result can be reached [26,29]:

$$Q = \omega[\epsilon_0 \epsilon_2(\omega)\overline{(\Re \boldsymbol{E})^2} + \mu_0 \mu_2(\omega)\overline{(\Re \boldsymbol{H})^2}] \tag{31}$$

Here, Q is the energy transferred into the material in unit time, with the electromagnetic wave essentially acting as a heat source [26,29].

2.3 Heat transfer dynamics and the two temperature model

2.3.1 General heat equation in an isotropic medium

In a solid, assuming translational motion and thermoelastic effects are negligible, heat transfer can be described by the following equation [18]:

$$\rho C_p\left(\frac{\partial T}{\partial t}\right) + \nabla \cdot \boldsymbol{q} = Q \tag{32}$$

The quantities in the equation carry the following physical meanings:

- ρ is the density of the solid (kg/m^3)
- C_p is the heat capacity at constant stress $(J/(kg \cdot K))$
- T is the absolute temperature (K)
- $\boldsymbol{q} = -k\nabla T$ is the heat flux by conduction (W/m^2)
- k is the thermal conductivity of the medium $(W/(m \cdot K))$
- Q contains other existing heat sources (W/m^3)

2.3.2 The two temperature model equations

Macroscopic temperature in a crystal lattice is defined through lattice vibrations. However, at femtosecond timescales, lattice atoms are approximately stationary, due to their mass. Therefore, the transfer of electromagnetic energy from a laser impulse directly to the crystal lattice in the form of heat is negligible. Due to electrons in metals having a much smaller heat capacity, the absorbed

energy initially only increases electronic temperature. Thus, the electronic and lattice temperatures can be modelled using two separate heat equations. The electronic heat equation [17,27,31-32]:

$$C_e \frac{\partial T_e}{\partial t} - \nabla \cdot (k_e \nabla T_e) = (-Q_{e-ph}) + Q_{other} \tag{33}$$

And the lattice heat equation [17]:

$$C_L \rho_L \frac{\partial T_L}{\partial t} - \nabla \cdot (k_L \nabla T_L) = (+Q_{e-ph}) + Q_{other} \tag{34}$$

Here, T_L and T_e are lattice and electronic temperatures, respectively. $C_e; C_L$ are electronic and lattice heat capacities, respectively, and $k_L; k_e$ are lattice and electronic heat conductivities, respectively. ρ_L is the density of the crystal lattice. Q_{e-ph} is the electron-phonon coupling, which describes the energy flux between electrons and lattice (see **illustration 6**) as a function of the electronic temperature, and the difference between electronic and lattice temperatures, trying to equilibrate the two [17,27].

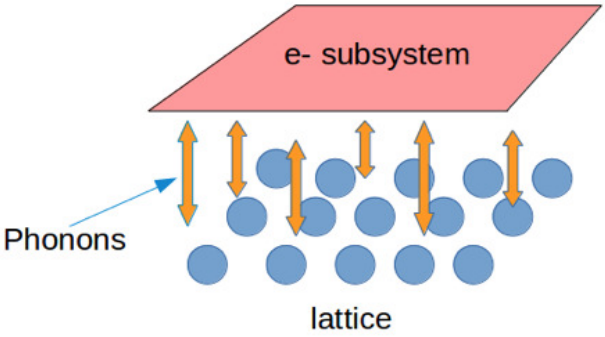

Illustration 6:

Electron-phonon coupling mediates energy transfer between electrons and the atomic lattice [8].

The final term in equations 33-34, Q_{other}, contains all other present heat sources. Of these, electromagnetic wave energy dissipation in the crystal was addressed previously, in chapter 2.1.5, and the Nottingham effect and resistive heating will be explained later, in chapter 2.3.5 and 2.4, respectively.

The two temperature model is inherently nonlinear. Namely, electronic heat capacity, heat conductivity and the electron-phonon coupling are all functions of the electronic temperature. It has been shown, that short laser impulses can raise the electronic temperature to tens of thousands of kelvins, while the atomic lattice temperature still remains almost unchanged, causing the electronic properties to change severely (see appendix D) [32].

2.3.3 Electronic heat capacity

The electronic heat capacity can be calculated as follows [32]:

$$C_e(T_e)=\int_{-\infty}^{\infty}\frac{\partial f(\varepsilon,\mu,T_e)}{\partial T_e}g(\varepsilon)\varepsilon\, d\varepsilon \tag{35}$$

Here, $g(\varepsilon)$ is the electron density of states at energy level ε and the function $f(\varepsilon,\mu,T_e)$ is the Fermi distribution function [32]:

$$f(\varepsilon,\mu,T_e)=\frac{1}{\exp\left(\frac{\varepsilon-\mu}{k_B T_e}\right)+1} \tag{36}$$

The function $\mu(T_e)$ is the chemical potential, and can be calculated, assuming conservation of the number of electrons N_e, from the following condition [32]:

$$N_e=\int_{-\infty}^{\infty} f(\varepsilon,\mu(T_e),T_e)\,g(\varepsilon)d\varepsilon \tag{37}$$

2.3.4 Electronic heat conductivity

Electronic heat conductivity can be calculated through the electronic heat capacity [31-32]:

$$K_e(T_e,T_L)=C_e(T_e)\tau_e(T_e,T_L) \tag{38}$$

Here, $\tau(T_e,T_L)$ is the total electron scattering time, defined as [32]:

$$\tau(T_e,T_L)=\frac{1}{AT_e^2+BT_L} \tag{39}$$

Here, $A=4.02\cdot10^{-4}(s/m^2\cdot K^2)$ describes electron-electron scattering, and $B=0.460(s/m^2\cdot K)$ describes electron-phonon scattering [31].

2.3.5 Electron-phonon coupling factor

The energy transfer from the electronic subsystem to the lattice subsystem can be expressed as follows [32]:

$$\frac{\partial E}{\partial t}=G(T_e-T_L) \tag{40}$$

Taking into account the high probability of reaching high electronic temperatures, where electrons scatter away from the Fermi surface, and the electron-phonon coupling factor is no longer constant, the electron-phonon coupling factor $G(T_e)$ can be expressed as follows:

$$G(T_e)=\frac{\pi\hbar k_B\lambda\langle\omega^2\rangle}{g(\varepsilon_F)}\int_{-\infty}^{\infty}g^2(\varepsilon)\left(\frac{-\partial f}{\partial\varepsilon}\right)d\varepsilon \tag{41}$$

Here, λ is the electron-phonon mass enhancement parameter, f is the Fermi distribution function, and $\langle\omega^2\rangle$ is the average square of the phonon frequencies [32-33].

2.4 Emission currents

2.4.1 Field emission and the Fowler-Nordheim model

Electron emission from metals is essentially quantum mechanical tunnelling through, or crossing over a potential barrier – the surface work function. The necessary prerequisite is that the tunnelling or crossing electron has sufficient energy. This can be obtained by absorbing photons, getting photoemission, heating the metal, getting thermionic emission, or by pulling the electrons out of the surface, using extremely high electric fields, getting field emission. Field emission is described with the Fowler-Nordheim model, given here in the following form [5-6,34-35]:

$$J_{FN} = \frac{a\beta_E^2 \boldsymbol{E}^2}{\phi t^2(y)} e^{\frac{-b\phi^{3/2}}{\beta \boldsymbol{E}} v(y)} \tag{42}$$

The entities in the equation have the following physical meanings:

- J_{FN} - emission current density (A/m^2)
- $\boldsymbol{E}$ - applied electric field (V/m)
- β_E - field enhancement factor, defined in chapter 2.2.2
- ϕ - surface work function (eV)
- a and b - first and second Fowler-Nordheim constants:

$$\begin{aligned} a &= 1.541434 \cdot 10^{-6} A \left(\frac{eV}{V^2}\right) \\ b &= 6.830890\, eV^{-\frac{3}{2}} \left(\frac{V}{nm}\right) \end{aligned} \tag{43}$$

- y - Nordheim parameter, defined as:

$$y = c_N \sqrt{\beta \boldsymbol{E}} / \phi \tag{44}$$

- Here, the constant c_N is defined as:

$$c \equiv 1.199985 \left(\frac{eV}{\sqrt{V\, nm}}\right) \tag{45}$$

- The correction factor $v(y)$ in the exponent can be approximated as [34]:

$$\nu(y) \approx 1 - y^2 + \frac{y^2}{3}\ln(y) \tag{46}$$

- The correction factor $t(y)$ is:

$$t(y) = v - \frac{2}{3} y \frac{dv}{dy} \tag{47}$$

The emission current density is essentially determined by local electric field and geometry, the latter entity represented by the field enhancement factor [5].

2.4.2 Thermal emission and the Richardson-Laue-Dushman model

At nonzero temperatures, thermionic emission occurs, and the Fowler-Nordheim model no longer describes emission currents accurately. Thermionic emission is described by the Richardson-Laue-Dushman model, given here in the form using the Schottky potential barrier model [5-6,35]:

$$J_T = A_{RLD} \cdot T_e^2 \cdot e^{\left(\frac{-\phi_{eff}}{V_t}\right)} \tag{48}$$

- A_{RLD} is the Richardson constant:

$$A_{RLD} = \frac{4\pi m_{el} k^2 e_0}{h^3} \simeq 120 \left(\frac{A}{cm^2 K^2} \right) \tag{49}$$

$$V_t = \frac{kT_e}{e_0} \tag{50}$$

Here, T_e is the electronic temperature, k is the Boltzmann constant, e_0 is the elementary charge, h is Planck's constant, and m_{el} is the mass of an electron. The Schottky potential barrier model describes the lowering of the potential barrier under an applied electric field [36]:

$$\phi_{eff} = \phi - \sqrt{\frac{q^3 \boldsymbol{E}}{4\pi\epsilon_0}} \tag{51}$$

Here, ϕ is the surface work function, and ϕ_{eff} is the lowered potential barrier [6,36].

The most important parameter affecting thermal emission is clearly the local electronic temperature. The heavily geometry-dependent field emission concentrates on small areas, where the local electric field is highest. Thermal emission, however, takes place on a severely larger surface area. That is the reason why, although it usually has a much lower emission current density, it cannot be ignored. Furthermore, thermal emission can create a positive feedback loop, as currents in the crystal cause resistive heating [5-6,18]:

$$Q_{resistive} = \boldsymbol{J} \cdot \boldsymbol{E} \tag{52}$$

In literature, the Richardson-Laue-Dushman model generally depends on the absolute temperature in the crystal, instead of the absolute electronic temperature. In pure thermal emission, without the effect of the laser impulses, this difference is irrelevant, as the electronic and atomic temperatures are in equilibrium, as demanded by laws of thermodynamics. In this work, the temperature determining thermionic emission densities is considered to be electronic temperature, because electron emission is determined by the average energy of the electrons, and the electronic and lattice temperatures are not in equilibrium for a considerable time.

2.4.3 The General Thermal Field equation

Similarly to how the Fowler-Nordheim model is only accurate at absolute zero temperature, the Richardson-Laue-Dushman model is only accurate at zero local electric field. This has caused the creation a number of modified versions of either model, containing correction factors for either temperature or field [6,34]. Both models have fairly recently been combined in what is known as the **General Thermal Field equation** (GTF). The GTF-model describes not only the cases with low electric field and a high temperature, and high electric field and low temperature, but also the intermediate cases. The GTF-equation calculates the emission current density, as follows [5-6,34]:

$$J_{GTF}(F,T_e)=A_{RLD}T_e^2 N\left(\frac{\beta_T}{\beta_F},\beta_F(E_0-\mu)\right) \tag{53}$$

Where:

$$N(n,s)\approx n^2\sum\left(\frac{1}{n}\right)e^{-s}+\sum(n)e^{-ns} \tag{54}$$

Here, β_F and β_T are energy slope factors for field and thermal emission, respectively:

$$\begin{aligned}\beta_F(E_m)&=\frac{-\partial}{\partial E}\theta(E_m)\\ \beta_T&=\frac{1}{k_B T_e}\end{aligned} \tag{55}$$

E_m is the maximum energy of emitted electrons and μ is the Fermi energy. E_0 Is an energy parameter, defined as [6,34]:

$$E_0=E_m-\frac{\theta(E_m)}{\frac{\partial}{\partial E}\theta(E_m)}=E_m+\frac{\theta(E_m)}{\beta_F(E_m)} \tag{56}$$

Here, $\theta(E)$ is the Wentzel-Kramers-Brillouin factor, accounting for quantum tunnelling, given by [6,34]:

$$\theta(E) \equiv \frac{\sqrt{2m}}{h} \int_{x_0}^{x_1} \sqrt{V(x) - E}\, dx \tag{57}$$

Here, $x_0; x_1$ are zeros and E_m is the maximum of the integrand. The correction factor $\sum(x)$, enabling one to avoid further calculations of the temperature correction factors in the Fowler-Nordheim equation, is given as [6,34]:

$$\sum(x) \approx \frac{1}{1-x} - x(1+x) + \frac{1}{4} x^3 (7x - 3) + \zeta(2) x^2 (1 - x^2) \tag{58}$$

Here, $\zeta(2)$ is the Riemann zeta-function [34].

2.4.4 Work function of crystal surfaces

It is well known from multiple experiments that, among other parameters, the surface work function ϕ – minimum energy required to extract an electron from the surface - is dependent on the crystal surface orientation [16]. Therefore, the height of the potential barrier, that the electrons have to cross or tunnel through in the emission process, and thereby also the emission current density on the surface, depends on the geometry of the crystal. This was clearly understandable for field emission, as the Fowler-Nordheim model depends on the field enhancement factor determined by geometry. Surface work function, however, affects all types of electron emission [12,37-39].

A good example of the crystal orientation dependent surface work-function affecting the emission current density pattern can be seen in **illustration 3** – on frame *a* the geometry is rather smooth, thus the field enhancement factor is fairly low everywhere, and the apparent emission pattern is determined mainly by surface work function. On frames *b-f* dominant ridges and tips appear due to a higher local field enhancement factor at the formed surface modifications.

It is important to note that crystal surface orientation can not always be exactly defined, for example, on atomically sharp tips. Furthermore, a very recent study showed a significant change in local work function values at surface defects. Using calculations based on density functional theory, defects of a few atoms in size on an otherwise flat copper surface, with a work function of 4.84 eV for the chosen surface orientation, lowered the local surface work function by up to 1.31 eV, in the presence of a high electric field [39-40].

2.4.5 Nottingham effect

Electron emission leads to energy exchange between surface atoms and electrons. Namely, electrons leaving the crystal can have energies higher or lower than the Fermi energy. If an electron is emitted from the surface, another electron from the crystal replaces it – electrons within a metal crystal, however, are approximately at the Fermi energy level, unless the crystal temperature is extremely

high. Thus, if the average emitted electron has a lower energy than Fermi energy, the replacement electrons will give some of their energy to the surrounding environment, thereby acting as a positive local heat source. Analogously, if the average emitted electron has a higher energy than Fermi energy, the surface is locally cooled. At low surface temperatures, then, the Nottingham effect is a positive heat source, and a negative heat source at higher temperatures. The net heat flux can be calculated with the following formula [5-6,27,40]:

$$Q_n = \frac{m_e}{2\pi^2\hbar^3}\int_0^\infty (\varepsilon-\mu) f(\varepsilon,\mu,T_e)\int_0^\varepsilon D(\varepsilon_x,|\boldsymbol{E}|,\phi)\,d\varepsilon_x\,d\varepsilon \tag{59}$$

Here, $f(\varepsilon,\mu,T_e)$ is the Fermi distribution, defined earlier with **equation 37**, and the term $\int_0^\varepsilon D(\varepsilon_x,|\boldsymbol{E}|,\phi)d\varepsilon_x$ is the integrated transmission probability of electrons with energy ε_x [40].

2.4.6 Space charge screening effect

The electrons emitted to the space between the electrodes modify the electric potential landscape and are a source of a secondary electric field, in addition to the applied field. This affects both field and thermionic emission, and **limits the maximum emission current density**. The electric field containing both space charge and applied field can be calculated with the Poisson equation [41-42]:

$$\nabla^2 V = \rho \tag{60}$$

Here, V is electric potential and ρ is charge density. High emission current densities, frequently passing $10^{12}\,A/m^2$, and electron-electron interactions, however, make exact solution of the Poisson equation computationally for non-equilibrium cases extremely impractical for even small time scales. In sources [41-42], analytical expressions for calculating space-charge-limited current densities have been derived for 1D-geometries. While having obvious limitations, the 1-dimensional models can be used for approximate estimations for geometries that are flat enough [41].

2.5 Solid mechanics

2.5.1 Electrostatic pressure and the Maxwell stress tensor

The local surface charge density in a conductor is induced by an external electrostatic field due to Gauss' law, and can be given locally with the following equation [5,19,43]:

$$\rho_{local} = \epsilon_0 \epsilon |\boldsymbol{E}_{\boldsymbol{norm}}| \tag{61}$$

Here, $\boldsymbol{E}_{\boldsymbol{norm}}$ is the surface norm of the electric field. The Lorentz force applied locally to the surface by the electric field is straightforwardly derivable as [5,19,43]:

$$\boldsymbol{F}_{\boldsymbol{local}} = \frac{1}{2}\rho_{local}\boldsymbol{E}_{\boldsymbol{norm}} \tag{62}$$

Taking into account the effect of the magnetic field as well, the above approach can be generalized by directly using the Maxwell stress tensor, to describe the effect of electromagnetic fields on mechanical momentum [5,43]:

$$T_{ij} = \epsilon_0 \epsilon \left(E_i E_j - \frac{1}{2}\delta_{ij}\boldsymbol{E}^2 \right) + \frac{1}{\mu_0 \mu}\left(B_i B_j - \frac{1}{2}\delta_{ij}\boldsymbol{B}^2 \right) \tag{63}$$

2.5.2 Constitutive relations for mechanical stresses in solids

Assuming large strains, such that deformations can exist after removing stresses, deformations are described by the relation between initial geometry X and deformed geometry x, through the deformation gradient F [5,44-45]:

$$dx = F\, dX \tag{64}$$

The deformation gradient F is a 2. order tensor that contains all the information about local deformations within the material. The Green-Lagrange strain tensor is defined through this as [5,44]:

$$\epsilon = \frac{1}{2}\left(F^T F - I \right) = \frac{1}{2}\left(C - I \right) \tag{65}$$

Here, I is the unit tensor, and C is the right-hand Cauchy-Green tensor. In a linearly elastic material, Hooke's law can be written in the following form [5,44]:

$$S = C_e : \epsilon_{el} = C_e : \left(\epsilon - \epsilon_0 - \epsilon_{th} \right) \tag{66}$$

Here, C_e is the elasticity tensor, ϵ_{el} is the Green-Lagrange strain tensor, ϵ_0 contains initial deformations, and ϵ_{th} contains thermal deformations, which, with α as the material's thermal expansion coefficient, T_{ref} as reference temperature and T_L as the material temperature, is calculated with the following formula [18]:

$$\epsilon_{th} = \alpha\left(T - T_{ref} \right) \tag{67}$$

S is the second Piola-Kirchhoff stress, a model used for describing large deformations. The Cauchy stress tensor s can be calculated from here as [5,45]:

$$s = |F| F S F^T \tag{68}$$

Cauchy stress is defined as force divided by the surface the force directly affects. From the Cauchy stress tensor, pressure can be calculated directly [5,45]:

$$p = -\frac{1}{3}\mathrm{trace}\left(s \right) \tag{69}$$

The deviatoric stress is defined as [5,45]:

$$s_d = s + pI \tag{70}$$

The von Mises effective stress can be calculated from this, as follows [5,44-45]:

$$s_{mises} = \sqrt{\frac{3}{2} s_d : s_d} = \sqrt{\frac{3}{2}\left(s_{ij} - \frac{(\mathrm{trace}(s))}{3}\right)\cdot\left(s_{ij} - \frac{(\mathrm{trace}(s))}{3}\right)} \tag{71}$$

The von Mises stress is a scalar value, independent of coordinate system, and is defined through the von Mises yield criterion, which sets a critical stress value, dependent on material. If the effective stress within the material is lower than the von Mises criterion, the deformations are elastic. If the effective stress is equal to the yield criterion, the deformations are plastic. Effective stress larger than the von Mises yield criterion would signify infinitely plastic deformations, and is therefore unphysical.

In the framework of this work, mainly thermal stresses are observed. As such, **the timescales, at which the dynamics of the mechanical entities given above become meaningful, are directly determined by the lattice heat equation.**

3 Method and model description

3.1 The finite element method

The finite element method is a mechanism for solving partial differential equations or equation systems numerically. The method relies on the discretization of the geometric domain the equation describes, subdividing it into smaller easily describable geometries – the finite elements – which make up the mesh. Every element in the mesh is essentially characterized by its vertex points x_i, where the value of the global solution Φ is exact. The mesh nodes consist of all vertices of all elements. The value of the global solution in some point within an element e is calculated with an interpolation polynomial, giving the local solution γ^e [5,46-47]:

$$\gamma^e = N_i^e \Phi_i + N_j^e \Phi_j + N_k^e \Phi_k + \ldots + N_r^e \Phi_r = \sum_i^r N_i^e \Phi_i \tag{72}$$

Here, element *e* has vertices $x_i^e \ldots x_r^e$, where Φ_i^e is the value of the global solution in the vertice x_i^e and N_i^e is the shape function associated with the vertex x_i^e, subject to the following constraint [5,46]:

$$N_i^e(x_j^e) = \begin{pmatrix} 1; i = j \\ 0; i \neq j \end{pmatrix} \tag{73}$$

The interpolation polynomial is used as the test function Λ to write the partial differential equation for the studied case in its weak formulation. In other words, shape functions are used to demand that the global solution would be exactly accurate at only the node points, as opposed to demanding that the global solution would be exactly accurate everywhere. Therefore, a finer discretization, leading to smaller elements and more node points, will generally lead to more accurate results [5,18].

For an example of the weak formulation, take a divergence equation [18]:

$$\nabla \cdot \Gamma = f \tag{74}$$

Its weak form [18]:

$$\int \Lambda (\nabla \cdot \Gamma)\, dV = \int \Lambda f\, dV \tag{75}$$

The weak formulation of the partial differential equation at hand in conjunction with the spatial discretization of the geometry leads to a system of linear equations. If the problem is well-defined, meaning there is a sufficient amount of boundary conditions, that system of equations leads to a unique solution, with values at the node points [5,18].

The finite element method is utilized in many software packages. The primary models described in this work are created with COMSOL MultiPhysics 5.3, which handles the building of simple or importing complicated geometries, subdividing them into elements, applying boundary conditions, and assembling and solving the resulting systems [18].

3.2 Finite element method combined with atomistic surfaces

3.2.1 Atomistic surfaces

Pure continuum models do not describe discrete particles, and cannot therefore directly include effects like surface diffusion. To account for this, a multiscale approach is necessary, using either a molecular dynamics or a kinetic Monte Carlo type algorithm for describing atomic movement, as the basis for the geometry, in which an enhanced continuum model is set up [5].

The Kinetic Monte Carlo model used for generating the atomistic surfaces used in this work is the **Kimocs** algorithm, in which atoms are placed in a rigid body-centered cubic lattice. Every atom has a probability to jump to a neighbouring vacant position in the lattice, described with an Arrhenius-type formula [48]:

$$\Gamma = \nu \cdot \exp\left(\frac{-E_m}{k_B \cdot T}\right) \tag{76}$$

Here, ν is the attempt frequency, a parameter fitted based on molecular dynamics simulations and the Debye frequency of the material, T is the temperature of the system, and E_m is the migration energy. The migration energies for all types of transitions are calculated beforehand with the Nudged Elastic Band method, using the tethering force approach [49] to properly describe diffusion in a rigid lattice. In the presence of a high external electric field, the surface atoms polarize, and the migration barriers are modified, giving a bias for the atoms to jump towards positions with higher local fields. This enables calculating the dynamics of surfaces, providing insight into the field emission pattern transformation at small surface deformations. For the surfaces presented here, example given in **illustration 7a**, a simple model of electric field influence on migration barriers was used [50]. The duration of a jump is calculated as [48]:

$$\Delta t = \frac{-\log u}{\sum_i \Gamma_i} \tag{77}$$

Here, $u = random(0;1]$, i is the number of all possible events, and Γ_i is the transition probability of the event i [48,50].

The molecular dynamics surfaces presented in this work were generated with LAMMPS. Molecular dynamics describes ensembles of particles, integrating Newton's equations of motion. Essentially, the Newton equation of motion of each atom is determined by the force enacted on that atom by all other atoms in the system. The interatomic potential used determining the force is Marinica's embedded atom method potential developed for modeling tungsten, which takes into

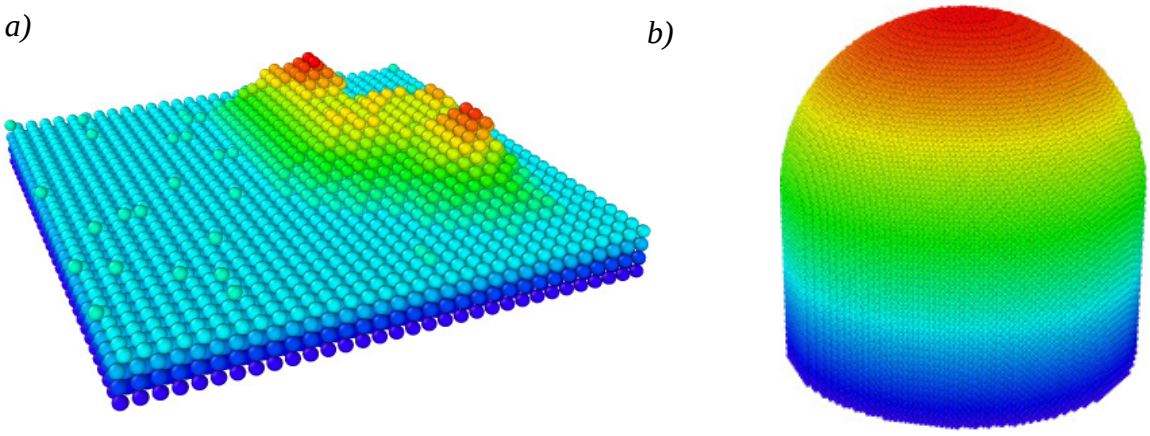

Illustration 7:

a) A snapshot from one of the surface dynamics simulations run with Kimocs. The colour code depicts the local z-coordinate.

b) Initial configuration for the molecular dynamics simulations presented here. The color code describes the z-coordinate. For computational efficiency, the model was downscaled to a radius of 50 nm, 5 times smaller than the continuum model geometry.

account the shielded Coulomb repulsion between the nuclei, and the chemical bonds between neighbouring atoms, and is given in the following general form [51-52]:

$$P_{interatomic}(\boldsymbol{r_1}, \boldsymbol{r_2}, \ldots, \boldsymbol{r_n}) = \sum_{i=1}^{n} \left(\sum_{j>i}^{n} \Phi(r_{ij}) + F(\rho_i) \right) \tag{78}$$

Here, Φ describes the interatomic pairwise interaction, ρ describes the effective electron density, F is the embedding function describing valence electrons, $\boldsymbol{r_i}$ are the location vectors of atoms, and r_{ij} is the distance between nuclei. Interatomic force is the negative gradient of the potential [52].

While Kimocs is used for describing a small ridge-like structure, molecular dynamics simulations are used for describing the entire tip, to see, if dislocations, notable surface defects or something else appears, at the initially estimated lattice temperatures with the corresponding timescale. An example of the initial geometric configuration can be seen in **illustration 7b**.

3.2.2 Screened Poisson surface reconstruction

Atomistic surfaces are not directly usable within the framework of the finite element method, which is why they have to be converted into continuum surfaces. This can be achieved with the **screened Poisson surface reconstruction**, which creates a watertight surface mesh from an oriented point set. The algorithm works in 2 phases. Firstly, the oriented point samples are transformed into a vector field, and then a scalar function is found, which has gradients that best describe the vector field found formerly [53].

Starting with an atomistic surface, essentially, a surface is built through all surface atom coordinates, and the surface normals are thereafter calculated at atom coordinates. These surface normals form a vector field $\boldsymbol{V}$. This vector field is injected into the following equation [53]:

$$Z(x) = \int \left(\nabla x(p) - \boldsymbol{V}(p) \right)^2 dp \tag{79}$$

Here, x is the scalar function with the appropriate gradients and p is a spatial integration parameter. The function $Z(x)$ is then minimized, by solving the Poisson equation [53]:

$$\Delta x = \nabla \cdot \boldsymbol{V} \tag{80}$$

The zero-level solution $x = 0$ corresponds to the desired isosurface, that approximately passes through the initial surface points [53]. An example of a reconstructed atomistic surface is given in **illustration 8a**.

3.2.3 Crystal surface orientation detection

In order to use the correct local surface work function value in calculations, the crystal faces constituting the surface must be mapped correctly. In most problems, however, the surface is too complicated to mark the defined crystal surface orientations exactly, while retaining reasonable computational efficiency, and the mapping can only be achieved approximately. Namely, an atomistic surface of a crystal consists of patches of differently oriented crystal faces, whereas the *geometric surface*, approximated from the same atomistic surface for use in the finite element method model, does not have discernible faces. In fact, the geometric surface can appear in unnatural configurations, such as perfectly spherical topology or spherical voids, which never occur in actual crystals [39].

Crystal planes are characterized by Miller indices, which describe the normal vector $\boldsymbol{n}_{CS}$ of each plane's specific orientation. The angle between the normal vector of the crystal plane h and the local normal vector $\boldsymbol{n}_{GS}$ of the geometric surface in the model is calculated with the following formula [39]:

$$\alpha_{GC}^{h} = \cos^{-1}\left(\frac{\langle \boldsymbol{n}_{CS}^{k}, \boldsymbol{n}_{GS} \rangle}{|\boldsymbol{n}_{CS}^{k}| \cdot |\boldsymbol{n}_{GS}|}\right) \tag{81}$$

The prerequisite of using this formula is that both vectors have to be described in the material coordinate system. If the $\alpha_{GC}^{h} = 0$, the vectors are parallel and the geometric surface coincides exactly with the crystal plane h. To mark the crystal surface orientation all over the geometric surface, the constraint on the angle is loosened, so that the local geometric crystal surface orientation is the orientation of the crystal plane h, if the angle α_{GC}^{h} is small enough. This is done

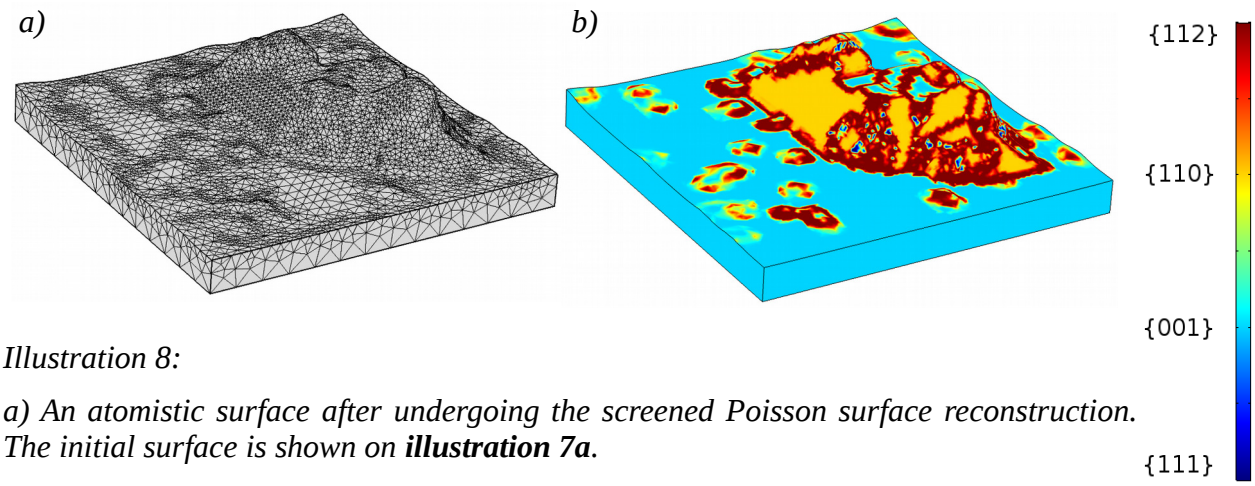

Illustration 8:

a) An atomistic surface after undergoing the screened Poisson surface reconstruction. The initial surface is shown on ***illustration 7a****.*

b) Crystal surface orientation detected on the reconstructed surface (a). For this surface, the {130} orientation was not calculated.

by using the smoothed Heaviside function, which in COMSOL MultiPhysics is defined as follows [39]:

$$H(\Phi,\delta)=flc2hs(\Phi,\delta)=\left(\frac{\Phi}{\delta}>-1\right)\left(\frac{\Phi}{\delta}<1\right)\times\left(\frac{1}{2}+\frac{\Phi}{\delta}\left(\frac{15}{16}-\frac{5}{8}\left(\frac{\Phi}{\delta}\right)^2+\frac{3}{16}\left(\frac{\Phi}{\delta}\right)^4\right)\right)+\left(\frac{\Phi}{\delta}\geq 1\right) \quad (82)$$

Here, δ is defined as the width of the transition region from 0 to 1. Crystal faces can thereafter be noted in the following manner, with $d\alpha$ marking the maximum value allowed for α_{GC}^{k} [39]:

$$\Phi^h=H(|\alpha^k|-d\alpha,\delta) \quad (83)$$

All crystal faces in a single crystal plane family are then summed together, as, for example, in the {100} crystal plane family [39]:

$$\Phi^{100}=\Phi^{(100)}+\Phi^{(010)}+\Phi^{(001)} \quad (84)$$

The work function at any point of the geometric surface can now be described with the following identity [39]:

$$\phi=\frac{1}{\sum_h \Phi^h}\sum_q \phi^q\Phi^q \quad (85)$$

Here, ϕ^q is the work function of the crystal surface orientation Φ^q. An example of the crystal face detection is given in **illustration 8b**.

3.3 Model geometry and imposed boundary conditions

3.3.1 Geometry

In order to coherently explain the boundary conditions, it is necessary to first explain where the boundaries are. The simulation box is rectangular, and into the simulation box a cylinder with a hemispherical cap is placed, distinguishing two domains, where material properties are different – the capped cylinder signifies tungsten, and the rest is vacuum, as seen in **illustration 9**. Tungsten properties used in the calculations are taken from sources [12], [54] and [55]. Exact geometry is given in appendix F.

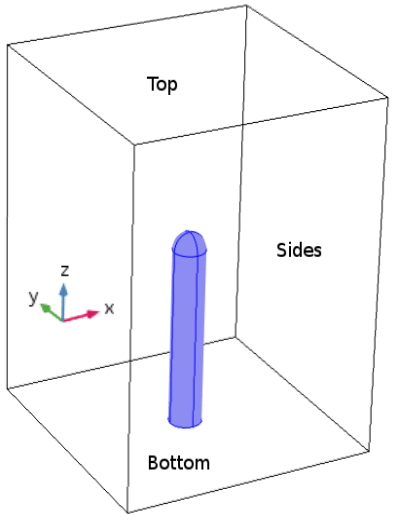

Illustration 9:

Geometry of one of the used models. Tungsten is marked blue. All 4 vertically placed faces are recognized as sides.

For the rest of this chapter, the terms *top*, *bottom*, and *sides* referring to the simulation box mark the

faces of the simulation box respectively shown in illustration 9. The axis orientation given here is also assumed further on.

3.3.2 Electrostatics

Static electric field is calculated only in the vacuum domain. The tungsten surface as well as the bottom of the simulation box are treated as an equipotential of 0 V. On the top of the simulation box, a planar horizontal equipotential is set, where the exact potential value is determined by the electric field estimated to be applied on the tip in the experiment. For the configuration given in illustration 9, the static potential is chosen to be 1500 V, yielding a maximum electrostatic field value of about 2 GV/m. On the sides of the simulation box, symmetry conditions are imposed in COMSOL by default [18]. The boundary condition placement is shown in **illustration 10a**.

To account for the space charge screen accumulating from emission currents, electrostatic field value at the tungsten-vacuum boundary has been limited to $1.8\,GV/m$, calculated with the GETELEC code, using the distance of the tungsten tip from the other electrode in the experimental setup [56-57].

3.3.3 Electromagnetic waves

Electromagnetic wave dynamics is calculated in both domains. The electromagnetic wave is modelled as a plane wave with a frequency of $\omega = 2.28\,PHz$ and an amplitude of $E_0 = 9800\,V/m$, values derived from the spectrum of the laser used in the experiment (see appendix C) [56,58]. Therefore, one of the sides is marked as an electromagnetic wave source, producing a linearly polarized electromagnetic wave, where the electric field components are:

$$\begin{aligned} E_x &= 0 \\ E_y &= 0 \\ E_z &= E_0 \sin(\omega t) \end{aligned} \tag{86}$$

The side opposite to the electromagnetic wave source, as well as the top and bottom sides, is marked as a perfect electric conductor [18]:

$$\boldsymbol{n} \times \boldsymbol{E} = 0 \tag{87}$$

The other sides are marked as perfect magnetic conductors [18]:

$$\boldsymbol{n} \times \boldsymbol{H} = 0 \tag{88}$$

The final parameter to address here is the complex relative electric permittivity of tungsten, which at the wavelength of the chosen electromagnetic plane waves is $\sigma_W = 5.01 + 19.53\,i$ [28]. The magnetic permeability is taken to be 1, as discussed in chapter 2.

3.3.4 Electronic heat transfer

The electronic heat transfer is only calculated in the tungsten domain. The electromagnetic wave energy dissipated into the metal can be used directly as a heat source in the entire tungsten domain. Similarly, the electron-phonon coupling function, exchanging energy between the lattice and electronic subsystems, is set as a heat source in the entire tungsten domain. Finally, the Nottingham effect is marked as a heat source on the boundary between vacuum and tungsten domains. The bottom of the tungsten domain is marked as a thermostat with temperature $T_{e0}=293.15\,K$. The electron-phonon coupling factor and electronic heat capacity values with respect to the electronic temperature are given in appendix D, and the electronic heat conductivity can be calculated with equation 39. The boundary condition and heat source placement is shown schematically in **illustration 10b**.

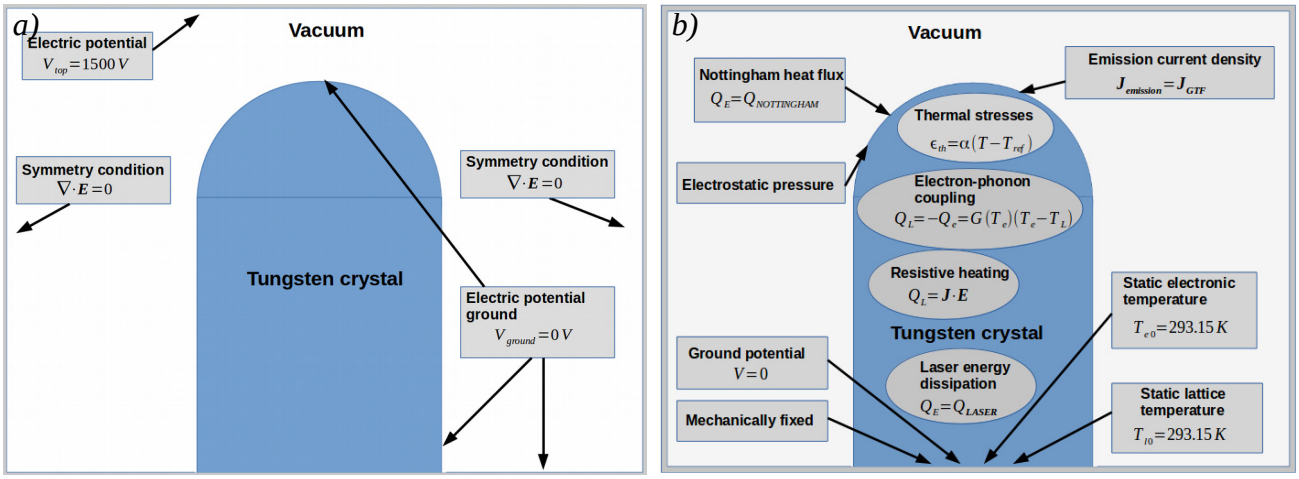

Illustration 10:

a) A schematic of the placement of boundary conditions for electrostatic field calculation.

b) A schematic of the placement of boundary conditions for electronic and lattice temperature subsystems, electrical currents and mechanical stresses.

3.3.5 Lattice heat equation

The lattice heat equation is only calculated within the tungsten domain. The heat sources are the electron-phonon coupling, giving energy to the lattice, and the power dissipation density arising from tungsten's electrical resistance to conductive currents. The bottom of the tungsten domain is given a static temperature of $T_{l0}=293.15\,K$, as seen in **illustration 10b**.

3.3.6 Electric currents

Electric currents are calculated only in the tungsten domain. The bottom of the tungsten domain is taken to have zero electrical potential. Emission currents are calculated on the tungsten-vacuum

boundary. The two boundary conditions put together generate conduction currents within the crystal. Boundary condition placement is schematically shown in **illustration 10b**.

3.3.7 Mechanical stresses in solids

Mechanical stresses are only calculated in the tungsten domain. The electrostatic pressure is calculated on the tungsten-vacuum boundary, and the tungsten bottom boundary is fixed. Thermal stresses are calculated in the entire tungsten domain. Boundary condition placement is schematically given in **illustration 10b**.

3.4 Conducted simulations

One simulation model was made, to calculate the laser energy deposition in the tungsten crystal, using the geometry described in chapter 3.3 (and appendix F) with boundary conditions specified in chapter 3.3.3.

Three different simulation models were created for calculating thermal behaviour in the tungsten tip, using the geometry specified in chapter 3.3 (and appendix F):

1. A two temperature model simulation, using the initially estimated laser energy deposition distribution, without calculating emission currents and electrostatic stresses. Boundary conditions are specified in chapters 3.3.4, 3.3.5, and 3.3.7.
2. A two temperature model simulation, using the initially estimated laser energy deposition distribution, including the calculation of emission currents, thermal effects related to emission currents, and electrostatic stresses. Boundary conditions are specified in chapters 3.3.2, 3.3.4-3.3.7.
3. A two temperature model simulation, using the calculated laser energy deposition distribution, including the calculation of emission currents, thermal effects related to emission currents, and electrostatic stresses. Boundary conditions are specified in chapters 3.3.2, 3.3.4-3.3.7.

Two simulation models were compiled for the calculation of emission patterns on atomistic surfaces – one for surfaces extracted from a molecular dynamics simulation, the other for surfaces extracted from the Kimocs simulation. Boundary conditions are described in chapters 3.3.2 and 3.3.6. The potential on the top face of the simulation box was chosen to be 40 V for the Kimocs surfaces, and 1000 V for the molecular dynamics surfaces. The exact simulation box sizes are given in appendix F.

4 Simulation results

4.1 Electromagnetic waves

4.1.1 Electromagnetic wave interaction with the tungsten tip

The laser propagation characteristics, seen in **illustration 11**, show, that the electric field within the material at any point during the irradiation is much smaller than the amplitude of the wave reflected back from the surface. It is very difficult to distinguish between the electric field amplitudes of the wave reflected directly back, seen on the lower left part of the frames showing timesteps 12-15 fs, and the part of the wave that did not interact with tungsten, seen on the upper right part of the frames showing timesteps 12-15 fs. Therefore, most of the laser impulse is reflected by the tungsten, and a significantly smaller part of the wave propagates in the metal.

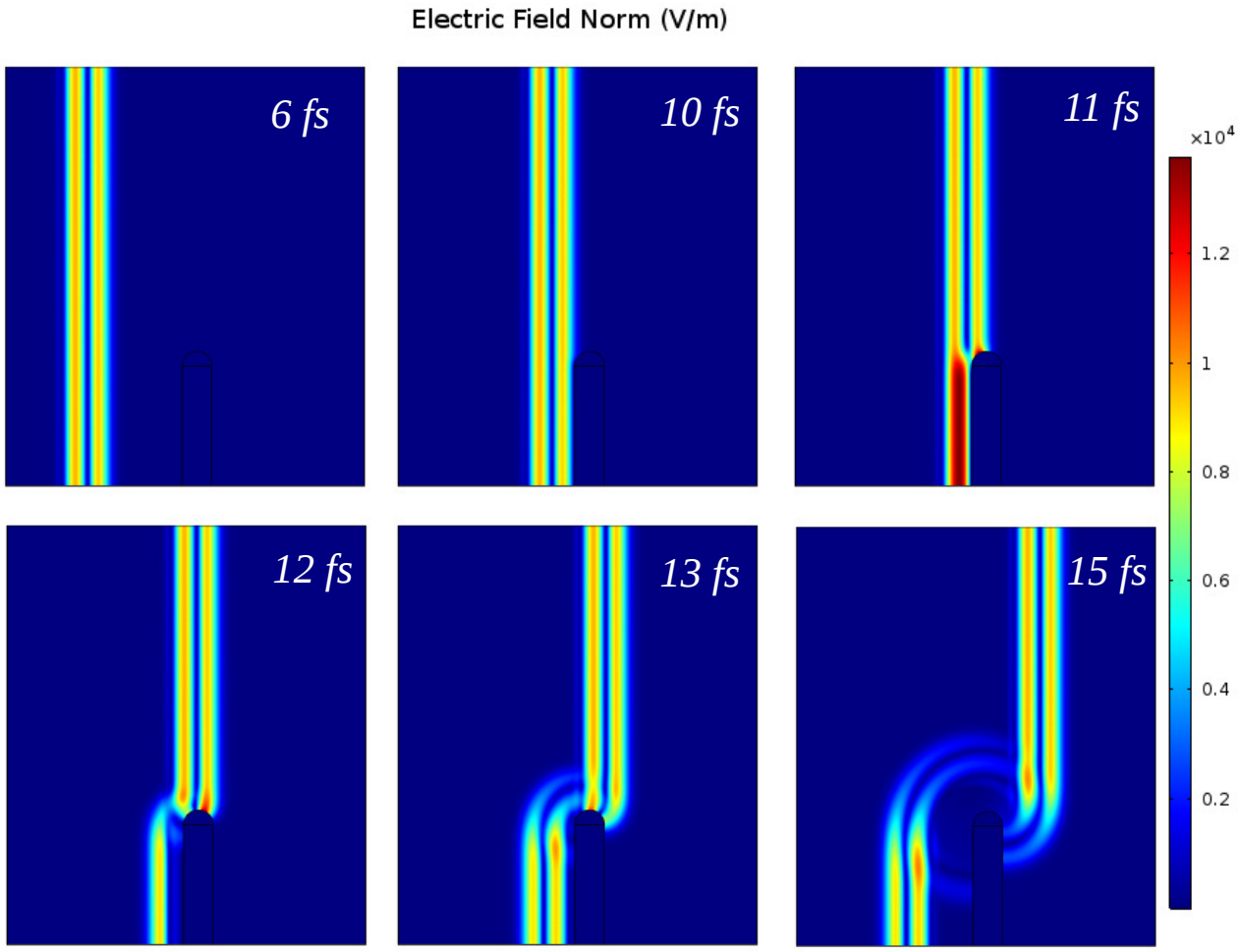

Illustration 11:

Snapshots of the laser beam propagation, with the impulse modelled as a single sine wave. The beam enters the frame from the left-hand-side at 0 fs.

4.1.2 Electromagnetic wave propagation in the tungsten crystal

Illustration 12 confirms the deductions made from illustration 11. The electric field in the crystal penetrates up to around 30 nm into the crystal, with the calculated **skin depth** being about **4.5 nm** – slightly smaller than the theoretical estimation of **6.12 nm** (see appendix E). The 14 fs and 15 fs frames hint, that diffracted waves seen earlier penetrate to some depth in the crystal on the shadow side of the tip, but the electric field there is still significantly smaller, than on the irradiated side. These three observations summed up lead to the conclusion, that the laser energy deposition only occurs in a very thin surface layer, and mainly on the irradiated side of the tip. This is also why the natural logarithm of the electric field is shown in **illustration 12** - the electric field norm value drops off very quickly in the crystal.

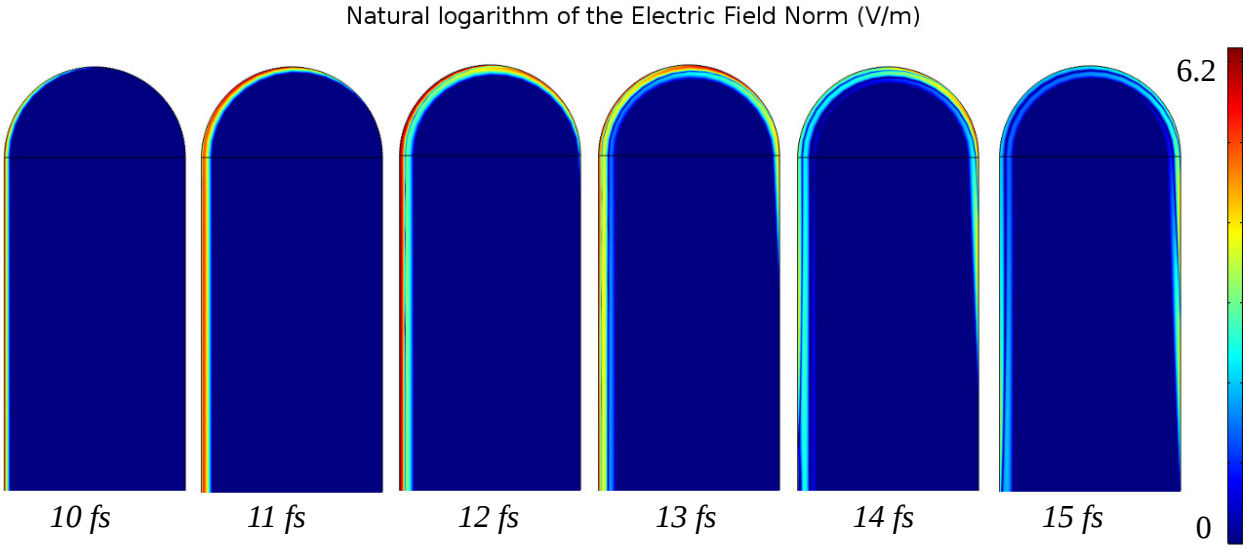

Illustration 12: Electromagnetic wave propagation in the tungsten crystal.

4.2 Behaviour of electronic and lattice temperatures

4.2.1 Time-averaged laser energy deposition

Calculating dynamical laser energy deposition requires extremely fine spatial and temporal resolutions. Coupling it with the calculation of temperatures, emission currents, as well as mechanical stresses, is therefore a very inefficient approach, leading to very long computing times. It is more effective to calculate the electromagnetic wave energy loss in the crystal separately, integrate it over one laser impulse period, and then use the result as a direct heat source in the electronic heat equation.

An initial estimation of the heating energy was done by Henriqué Vázquéz in the University of Helsinki, who used the OpenMaxwell software, and is presented in the form of a spatial grid, a slice of which, taken at the bottom of the cap of the tip, is shown in **illustration 13a**. Alas, given that the

energy deposition occurs in a very thin surface layer, that grid may be too coarse, and thus introduce anomalous behaviour, such as severely underestimated Nottingham cooling during and directly after laser irradiation, when the electronic temperature has not yet sufficiently equilibrated. To avoid this, the electromagnetic energy loss in the crystal over one impulse, derived from the results presented in the previous chapter, is scaled to match the initial estimation of the total absorbed impulse energy $E_{total} = 7.9514 \cdot 10^{-11} J$. With there being 1 impulse in every 10 nanoseconds, the heating power is $P_{heating} = 7.95\,mW \approx 0.044\,P_{laser}$ [9].

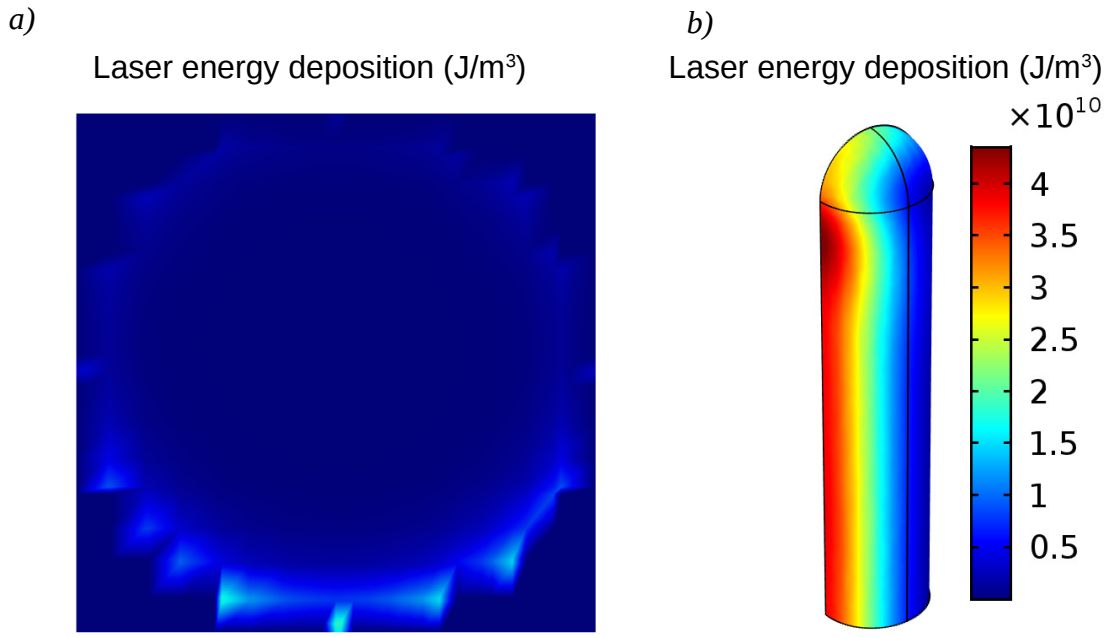

Illustration 13:

a) A slice of the initial estimation for laser energy deposition, assuming that the laser beam propagates upwards. It is clearly observable, that the interpolation function has sharp corners and edges along the heated surface, owing to resolution limitations.

b) Laser energy deposition along the surface, as calculated in the present work.

The calculated and scaled energy deposition distribution, integrated over one impulse, is shown in **illustration 13b**. In the experiment, topology changes were observed on the irradiated side of the cap of the tip. The energy deposition is the highest just below the cap domain for both distributions.

4.2.2 Electronic and lattice temperature behaviour in a simplified model

The magnitude of the effect, that emission currents may have on the two temperature system, requires first looking at a simplified model, where only the laser energy deposition and the two temperature model are included. For such calculations, without a surface heat source, the initial estimation for laser energy deposition is sufficient. In **illustration 14**, it is firstly seen, that the average electronic temperature is very quickly ramped up by the laser, which then slowly heat up

the atomic lattice. Over the single laser impulse, and the subsequent equilibration time until the next impulse, the maximum lattice temperature at the cap reaches **2891.3 K**, which is 804 K below the melting temperature of tungsten – 3695 K [59]. The maximum lattice temperature is reached **3.49 ps** after the beginning of the cycle. By 10 ps after the laser impulse the electronic and lattice temperatures have equilibrated.

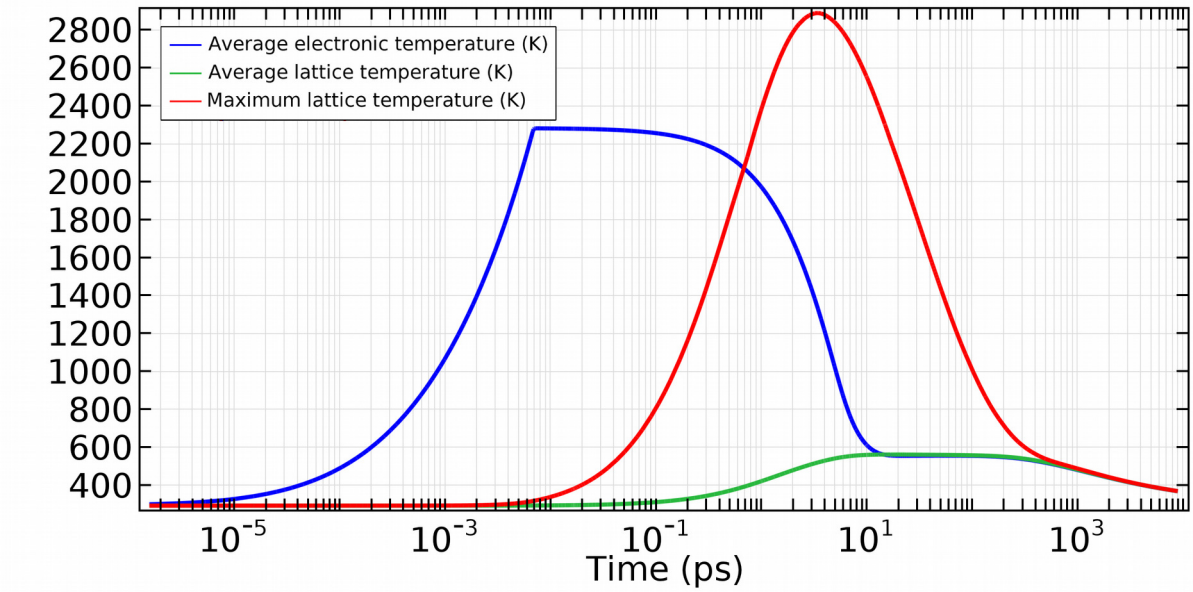

Illustration 14:

Temperature behaviour over a single impulse in the cap of the tip, using the simplified two temperature model. Time is in logarithmic scale.

It can also be seen in **illustration 14**, that the initial temperatures are lower than the final temperatures on the given timescale. As the system could not equilibrate to its initial temperature, it had had a net gain of energy from this single impulse by the time a new cycle should set off. Therefore, in a regime of repeated laser pulses, the equilibrium lattice temperature is higher than room temperature, and the maximum reached lattice temperature is also higher. This can be seen in **illustration 15**, which shows maximum lattice temperatures from a simulation run of repeated impulses – possible because of the relative simplicity of this particular model.

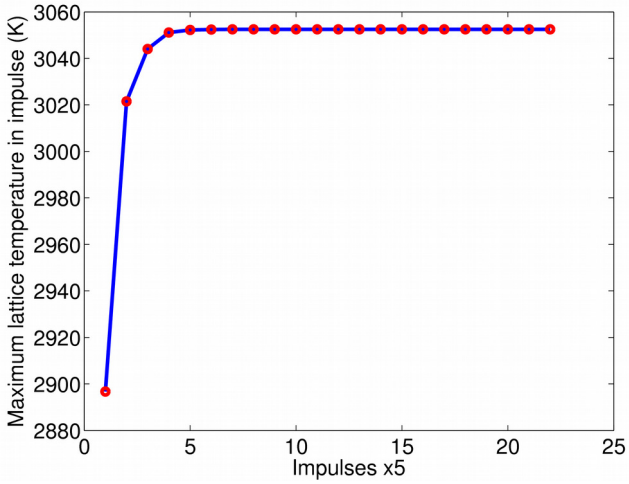

Illustration 15:

Maximum lattice temperatures in the cap of the tungsten tip in a sequence of impulses.

The maximum lattice temperature reached in the cap after an impulse climbs to

approximately **3054 K after 30 impulses** and stays there. The equilibrium temperature – for both electronic and lattice subsystems - just before the impulse is **547 K**.

4.2.4 Lattice temperature behaviour with the addition of the GTF equation, using the initial laser energy deposition distribution

The addition of emission currents to the two temperature model adds additional thermal effects: resistive heating, expected to heat the crystal, and the Nottingham effect, expected to cool the laser-irradiated surface of the crystal. This is further complicated by the work function of the surface being dependent on the crystal surface orientation, which is also in effect here, but is discussed in detail further on.

The temperature behaviour in the cap for a single impulse, given in **illustration 16**, shows, that the maximum lattice temperature reaches **3068.8 K – nearly 200 K higher, than in the model without emission currents**. Furthermore, this maximum lattice temperature is reached **3.01 ps** after the beginning of the cycle – half a picosecond earlier, than in the model without electron emission effects. The temperatures in both models are approximately equal after the 10 ns equilibration period.

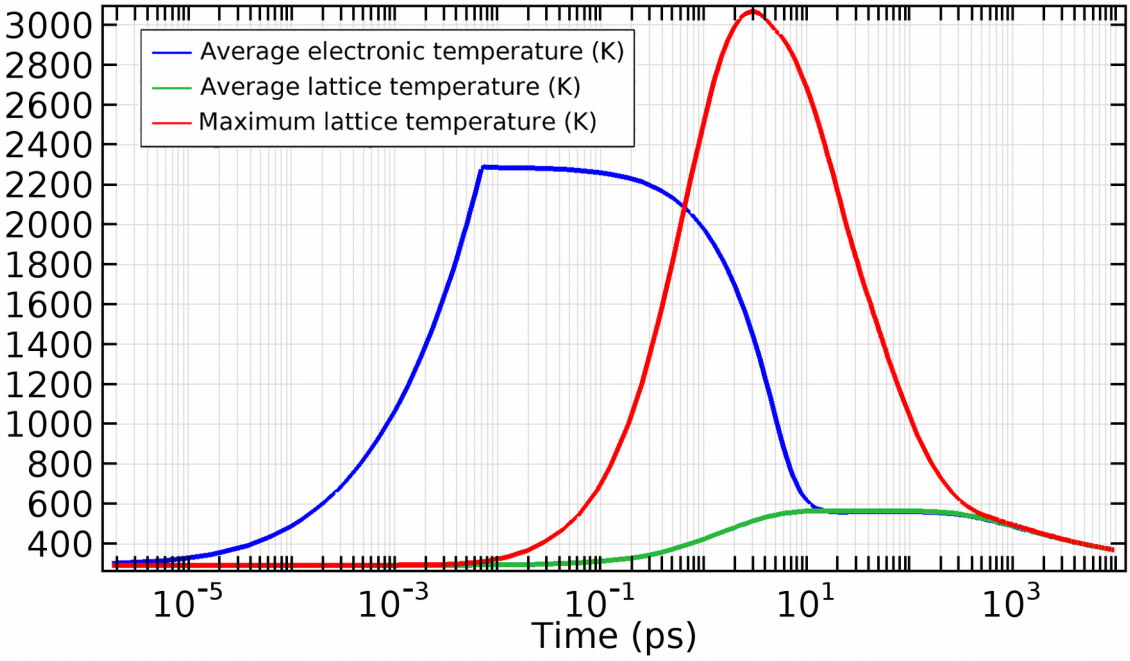

Illustration 16: Temperature behaviour in the cap over a single laser impulse cycle with the GTF model included.

The spatial lattice temperature distribution evolution over the first 160 ps after a laser impulse, given in **illustration 17**, shows, that the laser energy deposition is concentrated to a small part of the tip, centered approximately around the bottom of the cap of the tip. **Lattice temperatures of**

more than 2500 K only appear in a depth of up to 15 nm from the surface, and disappear entirely within 10 ps. This allows the prediction, that plastic deformations due to thermal stresses, should any arise, as well as Nottingham cooling, which occurs at high temperatures, are concentrated to a very small area of the tip.

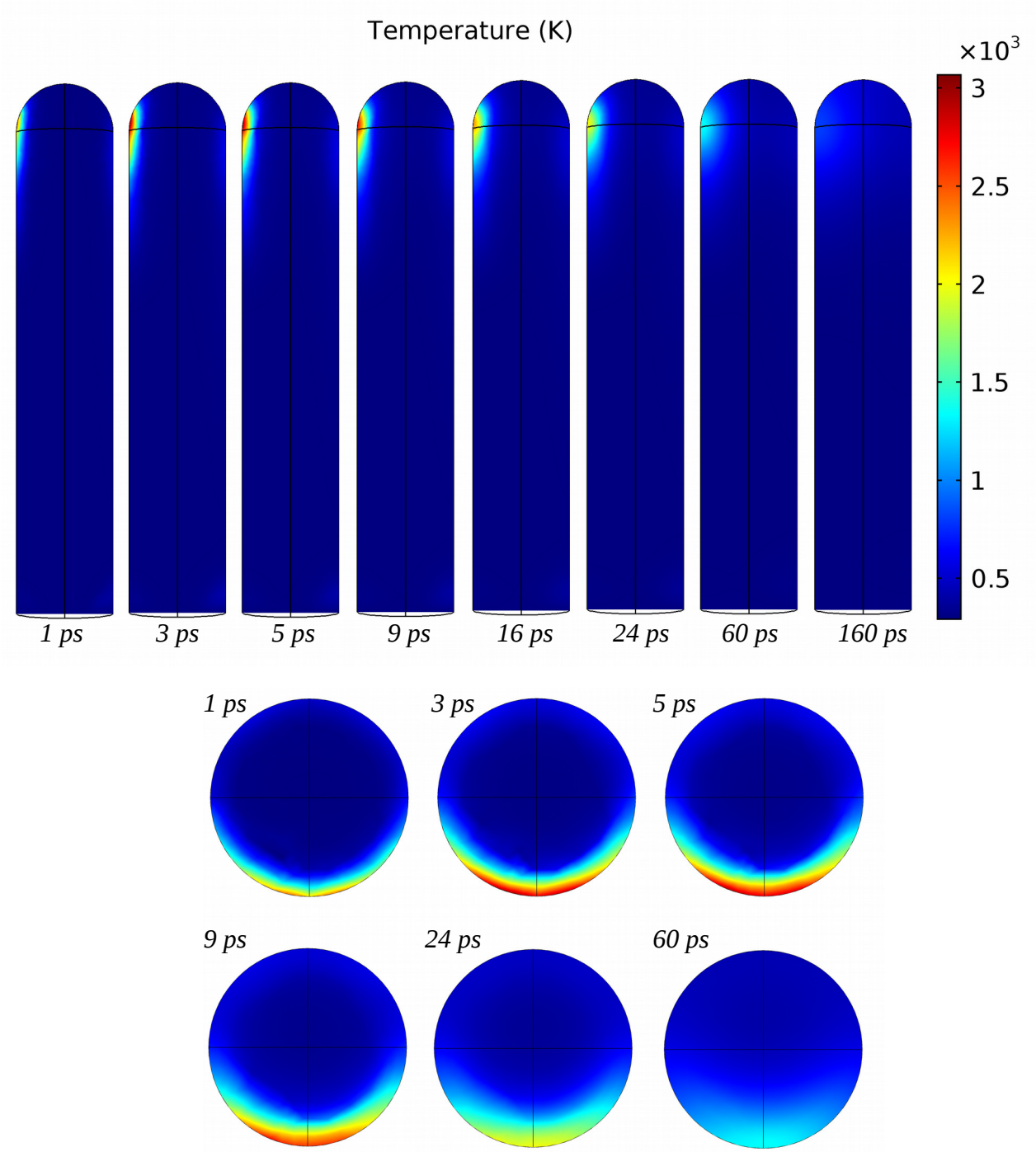

Illustration 17:

Lattice temperature distribution evolution over a single impulse, sliced top-down from the middle of the tip for the upper series of snapshots, and horizontally at the bottom of the cap domain for the lower series of snapshots.

4.2.5 Lattice temperature behaviour with the addition of the GTF equation, using the calculated laser energy deposition distribution

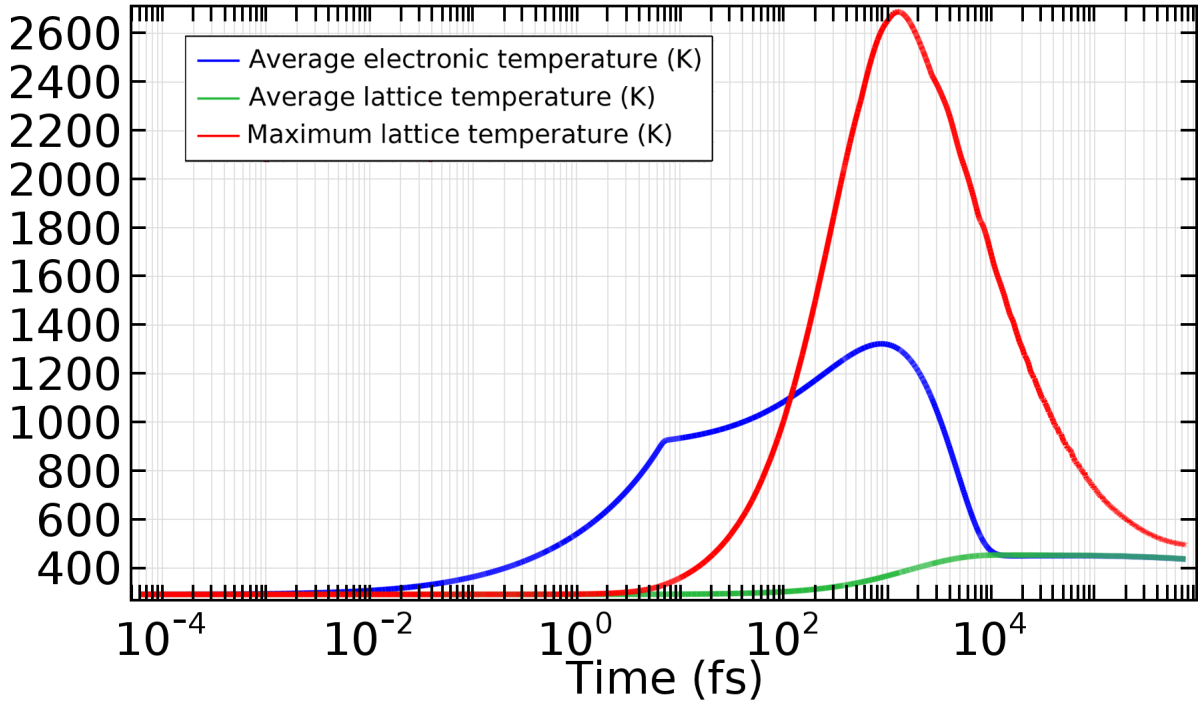

Illustration 18:

Temperature behaviour in the cap of the tip in a single impulse cycle with the calculated laser energy deposition distribution, shown on illustration 13b.

Using the laser energy deposition distribution calculated in chapter 4.1, the maximum temperature reached is **2689.7 K**, occurring **1.26 ps** after the laser impulse, just after the average electronic temperature peaks, as seen in **illustration 18**. Temperatures above 2500 K exist for 1.6 ps, within 5 nm of the crystal surface – much narrower, than in the results in chapter 4.2.4. Lattice temperature

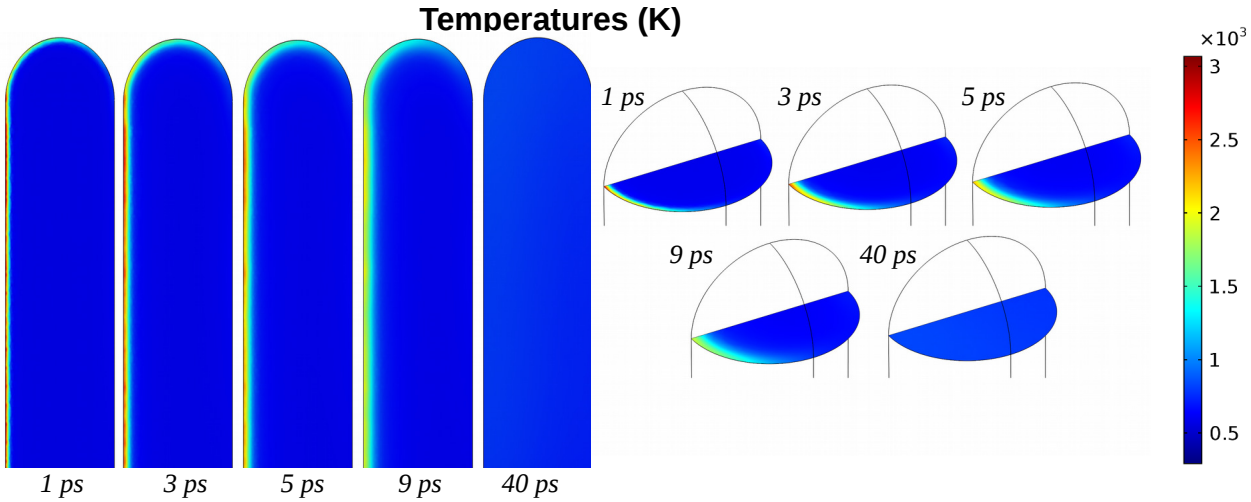

Illustration 19:

Lattice temperature distribution snapshots from the simulation run with the calculated energy deposition distribution. Only half of the tip profile is shown here on the right.

does not reach an equilibrium, because this particular calculation was shorter than a full cycle. The spatial lattice temperature distribution evolution is presented in **illustration 19**.

4.2.6 The effect of different energy deposition distributions on electronic temperature

The two laser energy deposition distributions produce significantly different results. The calculated energy deposition distribution affects a very thin surface layer. That is why the maximum electronic temperature is twice as large with the calculated energy deposition, as seen in **illustration 20**. The heat is then conducted further into the tip, which is why the average electronic temperature in the tip keeps rising for a longer time, finally peaking at 1 ps. It is also why the maximum lattice temperature in the cap of the tip is reached much earlier, as seen in **illustration 21**.

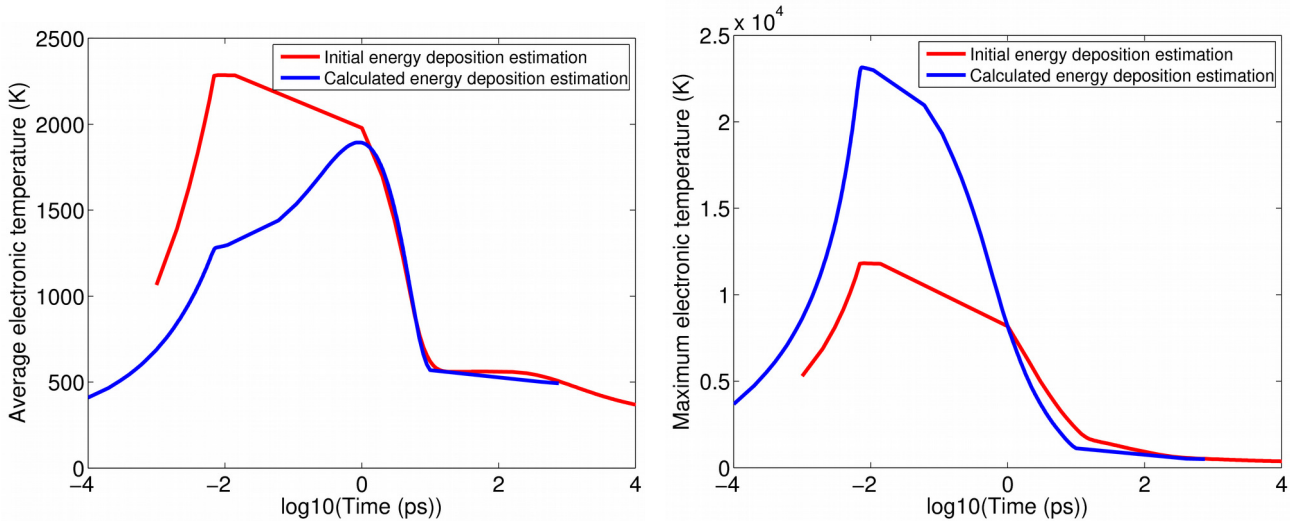

Illustration 20:

The behaviour of electronic temperature in the cap of the tip with 2 different energy deposition distributions.

The initial energy deposition estimation leads to energy being stored in a larger volume of the tip, which is why it reaches half the maximum, but double the average electronic temperatures, and why the average electronic temperature ceases to rise after the laser impulse passes – there heat fluxes in the tip are not that large. Since the calculated energy distribution is scaled to equal the impulse energy of the initial estimation, the

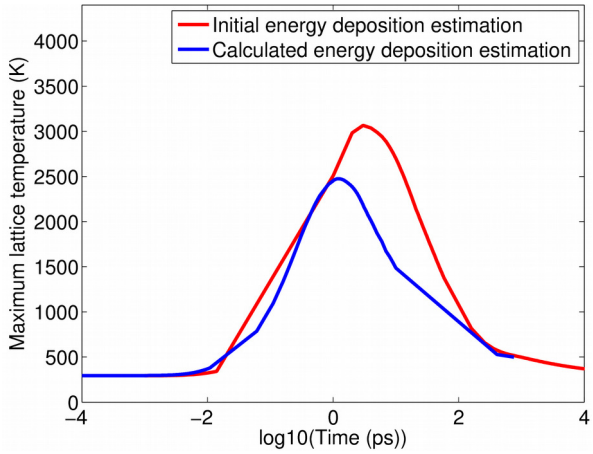

Illustration 21:

Maximum lattice temperature behaviour in the cap region of the tungsten tip with both energy deposition distributions.

average temperatures in the cap domain of the tungsten tip are equal after about 1 ps from the beginning of the laser impulse.

4.3 Mechanical stresses

The maximum stress reached in the entire tip over the course of a single laser impulse is **5.8 GPa**, using the calculated energy deposition distribution, and **8.8 GPa**, using the initial laser energy deposition distribution, with the evolution of either shown in **illustration 22**, along with the average stresses. The yield strength of tungsten is generally in the order of magnitude of **0.1 GPa**, and decreases with temperature, as seen in **illustration 23.** It is therefore clear, that **plastic deformations occur in the tungsten tip**, because the stresses in the tip surpass the yield strength.

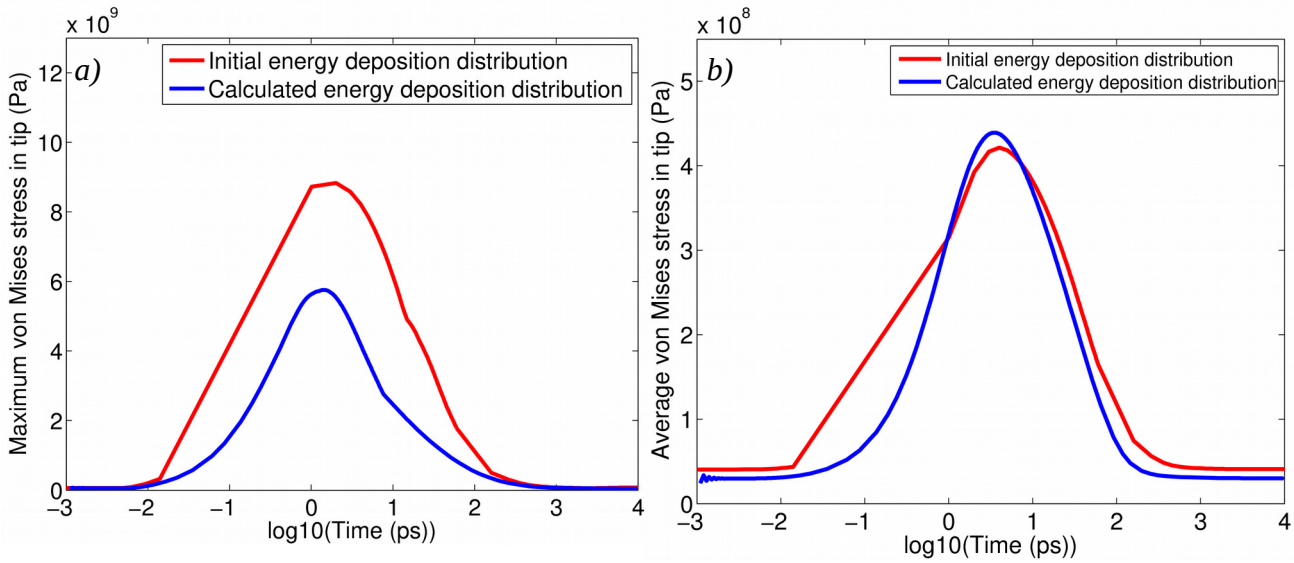

Illustration 22:

a) Maximum stress behaviour in the entire tip.

b) Average stress behaviour in the entire tip.

Mechanical stresses peak, when lattice temperatures peak, therefore thermal stresses dominate the stress distribution in the tip, as can also be seen in **illustration 24**, and **plastic deformations occur at high-temperature areas**. That is supported by the fact, that the maximum stress in the tip due to the electrostatic field alone is **57 MPa**, which does not reach the material yield strength. Illustration 22 also reveals, that the average stresses for both laser energy deposition distributions is approximately

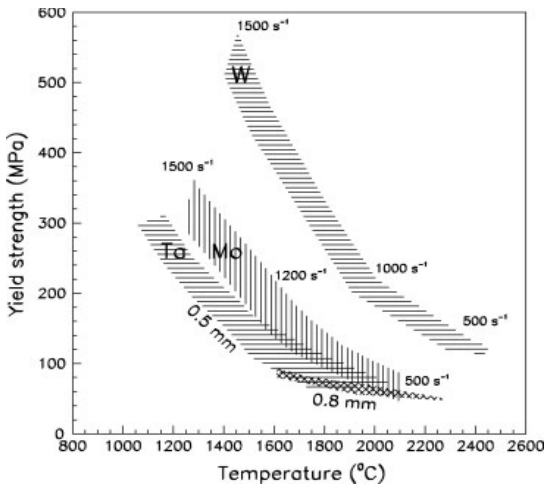

Illustration 23:

Yield strength of tungsten at high temperatures [60].

equal, but the maximum stresses are higher in the model, where higher lattice temperatures are reached.

The calculated laser energy deposition distribution causes plastic deformations on the surface all along the laser-irradiated side and over the top of the tip. The initial estimation for laser energy deposition is more focused near the cap of the tip, therefore plastic deformations are concentrated to the cap area.

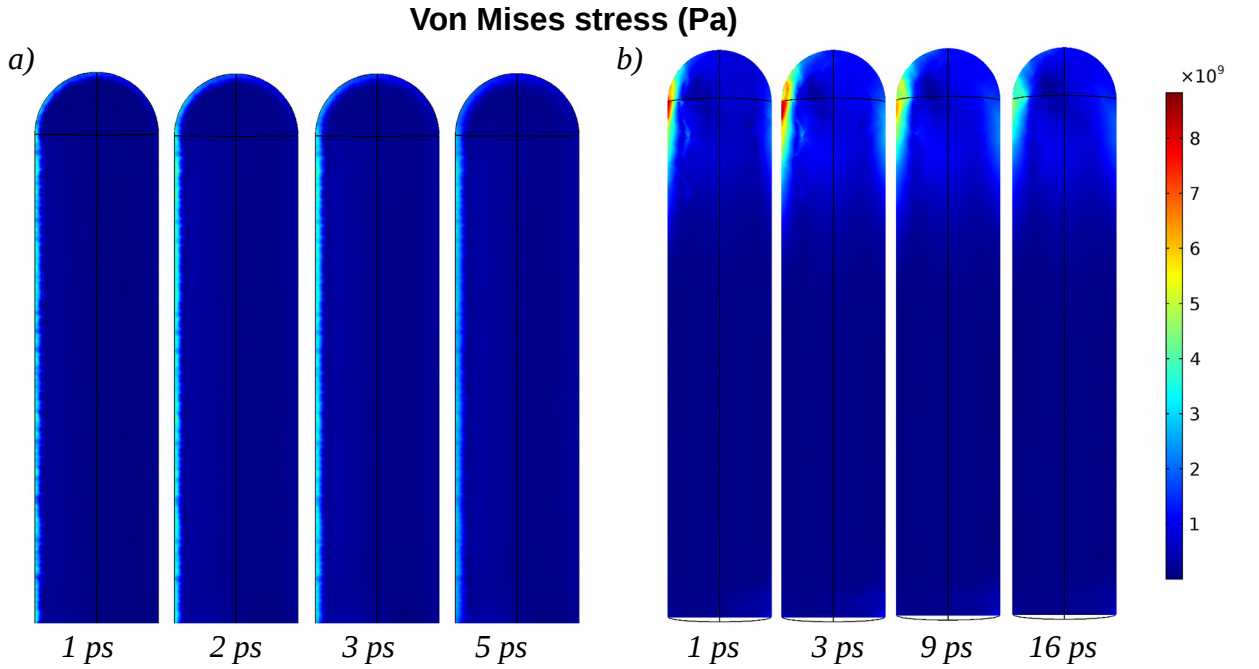

Illustration 24:

a) Stress distribution evolution within the tip with the calculated laser energy deposition distribution

b) Stress distribution evolution within the tip with the initial laser energy deposition distribution

4.4 Emission pattern evolution

In the experiment, one of the main methods for observing dynamical changes in surface topology was field emission microscopy, as was shown back in **illustration 3**. The emission pattern, calculated on an ideal hemispherical surface in the present model, matches excellently with the experimentally measured initial emission pattern, as is shown in **illustration 25 frames a-b**.

To see surface evolution in the form of atom migration, Ekaterina Baibuz from the University of Helsinki created a molecular dynamics model of a hemispherical tungsten tip, wherein the tip was heated up to 3200 K, kept at that temperature for 950 ps, and then cooled down again. The surface configurations from different phases of the simulation were extracted and transformed into

continuum surfaces. The field emission patterns from these surfaces are shown on **illustration 25 frames c-f**, and the phases are specified in the corresponding description.

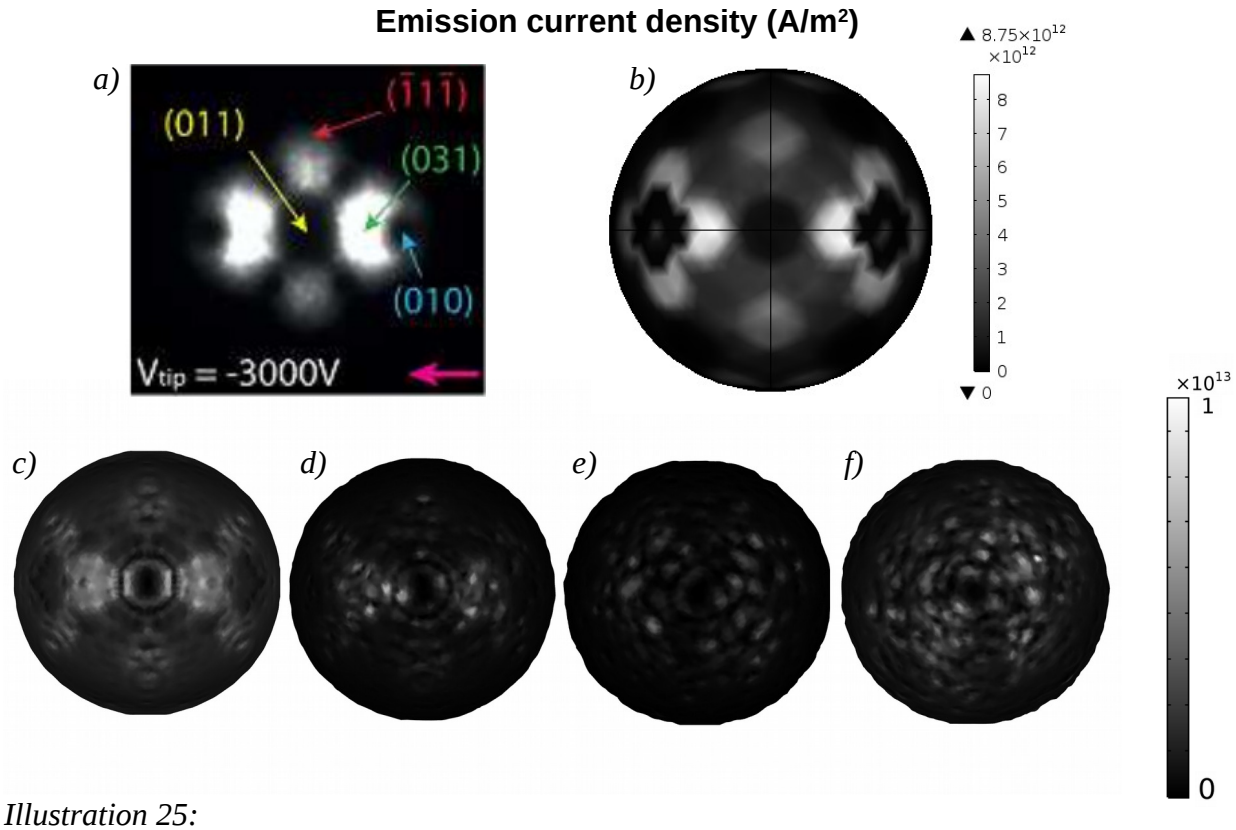

Illustration 25:

a) Experimentally measured emission pattern for a smooth initial tip [9].

b) Calculated emission pattern for an ideal hemispherical surface.

c) Emission pattern on the initial, almost hemispherical atomistic surface at room temperature.

d) Emission pattern on the atomistic surface after heating from room temperature to 3200 K.

e) Emission pattern on the atomistic surface after keeping the tip at 3200 K for 950 ps.

f) Emission pattern on the atomistic surface after cooling down to room temperature.

The emission patterns shown on **illustration 25** initially follow the crystal surface orientation, but that regularity disappears by **frame e**, after which the emission pattern is randomized. The emission pattern convergence to ridges, as was observed in the experiment, does not occur.

The difference of behaviours of the emission pattern evolutions in the experiment and on the surfaces extracted from the molecular dynamics simulation is likely due to the fact, that the simulation did not take the effect of the electrostatic field on surface dynamics into account. Nevertheless, in both cases, locally dominant emission sites emerged.

To observe the behaviour of one such site, involving the effect of the electrostatic field on surface diffusion, Ekaterina Baibuz simulated a surface protrusion evolution at 2500 K under an applied

field of 0.5 GV/m with the Kimocs algorithm. A snapshot of the atomistic simulation geometry was given on **illustration 7a**.

On **illustration 26**, the changes in emission patterns and the respective height maps are shown. It is evident, that the bias for atoms to migrate in the direction of higher electric fields results in the initial emitting structure growing in size. However, the local emission current density can drop significantly, for example, by **42%** between frames 3 and 4, when the growth reduces the local field enhancement factor.

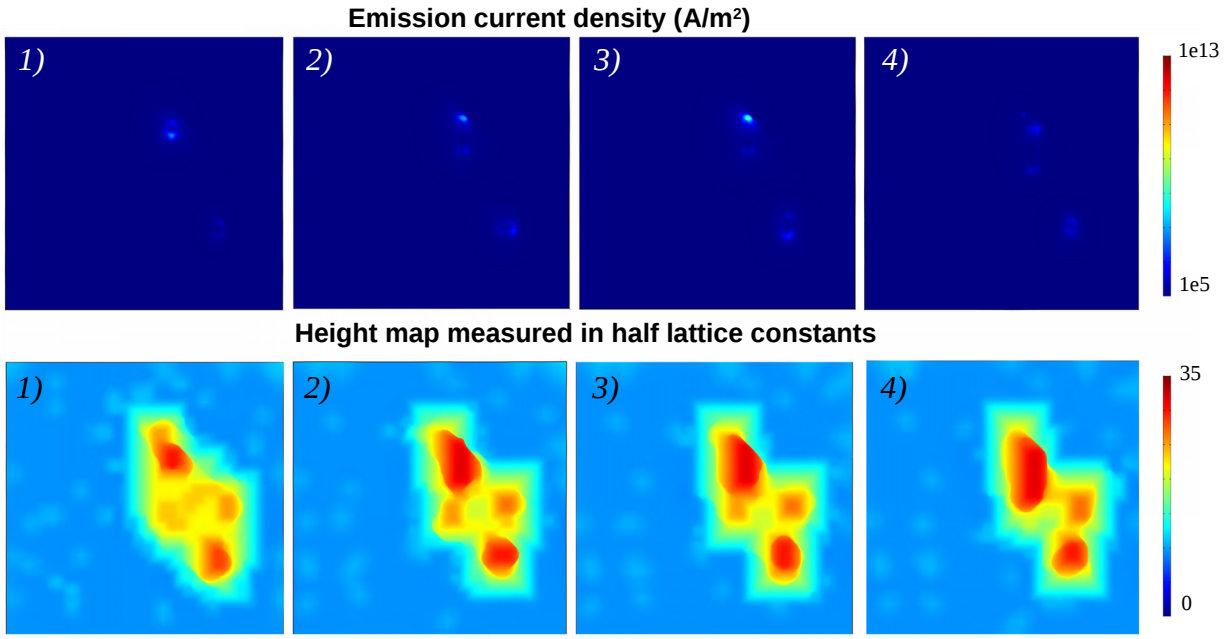

Illustration 26:

Emission pattern transformation on a locally dominant field emission site. The number in the upper right corner of each frame marks the order of the frames in the simulation time.

Atoms migrating towards areas with higher electric fields, and thereby reducing the local field enhancement factor there, may lead to another nearby structure becoming the locally dominant emission site, shifting the preferred atomic migration direction from the first protrusion to the new dominant tip. Due to that, a new emission site may form between the 2 tips, as seen on **illustration 26** frames 2-4, and a ridge-like structure can emerge, before eventually transforming into a sharper larger emitter.

Should the mechanism of joining emission sites work in a larger scale, given sufficient temperatures by the laser heating, it can explain the emergence of single dominant emission sites in the experimental observations, as highlighted on **illustration 27**.

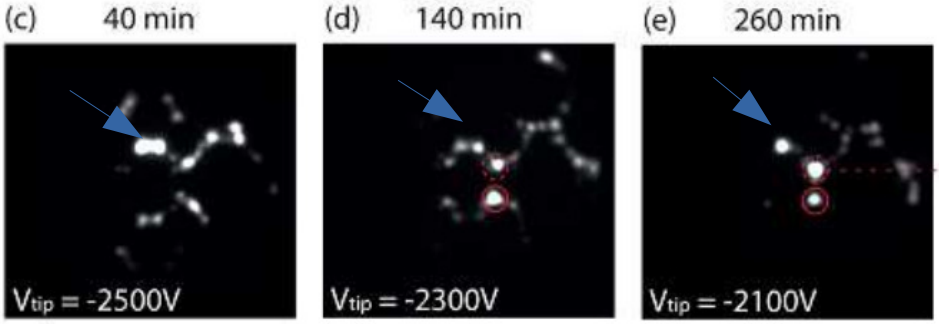

Illustration 27:

The pair of emission sites highlighted on frame c is dimmer on frame d, and on frame e, only one bright emission site remains [9].

5 Discussion

The lattice temperatures reached with the two temperature model simulations are not sufficient for melting the surface of the tungsten tip. However, coupled with the electrostatic field, the thermal behaviour in the tip creates mechanical stresses, that are large enough for plastic deformations to occur in the surface layer of the laser-irradiated area of the crystal.

The tungsten tip is extremely likely to be a polycrystal, owing to its size, and the initial emission pattern very distinctly followed different crystal surface orientations. Mechanical stresses have been shown to concentrate in grain boundaries [61-62], which means that the deformations, caused by thermal and electrostatic stresses, would be concentrated on the boundaries between the crystallites, and the probability for surface protrusions to appear is higher, where the grain boundaries intersect with the crystal surface. This would explain the field emission pattern convergence on the edges of the initially observable crystal faces.

The further transforming of the emission pattern into singular dominant emission sites can be explained with the Kimocs model – neighbouring field emitters merge in the presence of a high electric field at relatively high surface temperatures.

Based on the results presented in this thesis, a mechanism can be proposed, that explains the laser-driven surface faceting phenomenon. **Firstly, the mechanical deformations, caused by the laser energy dissipation in the crystal surface and the electrostatic field, converge at the grain boundaries, thereby determining, where the emission sites start occurring. Secondly, the emitters start to interact with each other, modifying local surface diffusion in the electric field, first leading to the formation of ridges, and then locally dominant emission sites.** The mechanism is shown in sequential steps on illustration 28.

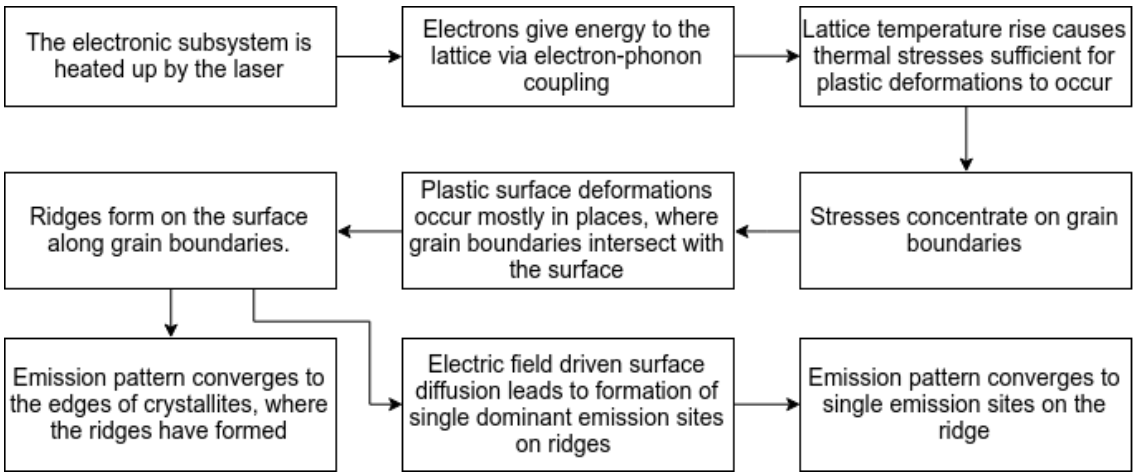

Illustration 28:

Sequence of the phases of the proposed mechanism for laser-induced surface changes.

6 Conclusion

A computational continuum model of a microscopic laser-irradiated tungsten tip was created, based on the general two temperature model, including electromagnetic wave propagation, emission current dynamics, and mechanical stress calculations. That model was coupled with atomistic simulations, using crystal surface detection and screened Poisson surface reconstruction algorithms, to observe the changes in emission patterns, owing to surface diffusion. The results of the continuum model pointed to significant plastic deformation occurrence in the tungsten tip, caused by thermal stresses. The results of the calculations done with the coupled continuum and atomistic models showed an electric field driven merging mechanism between neighbouring emission sites, that produces ridges, that later transform into dominant emitters due to the same mechanism. The plastic deformations and the tip merging process were combined into a proposed general mechanism, that explains the experimental observations made by H. Yanagisawa *et al.*

7 Acknowledgements

Firstly, I would like to thank my supervisor, Vahur Zadin, for excellent guidance. I am also grateful to Ekaterina Baibuz and Andreas Kyritsakis for smooth cooperation and insightful conversations. I thank Simon Vigonski, Kristian Kuppart, and Priit Priimägi for engaging and fun daily interaction at the lab. I would like to express gratitude towards the entire Intelligent Materials and Systems lab collective, headed by Professor Alvo Aabloo, for creating a pleasant environment for conducting research. Finally, I would like to thank my family and friends, who supported me during the writing of this thesis.

8 References

[1] Grudiev, A., Calatroni, S. & Wuensch, W. “New local field quantity describing the high gradient limit of accelerating structures.” Phys. Rev. ST Accel. Beams **12**, 102001, 2009

[2] C. Z. Antoine , F. Peauger , F. Le Pimpec, “Erratum to: Electromigration occurences and its effects on metallic surfaces submitted to high electromagnetic field: A novel approach to breakdown in accelerators“ **670**, 79-94, 2012

[3] K. Peach *et al.* “Accelerator science in medical physics”, Br J Radiol **84,** 2011

[4] F. Djurabekova, S. Parviainen, A. Pohjonen, and K. Nordlund, “Atomistic modeling of metal surfaces under electric fields: Direct coupling of electric fields to a molecular dynamics algorithm”, Phys. Rev. E **83**, 026704, (2011)

[5] R. Aare, “Modelling a Cu atomistic nanoemitter relaxing in a high electric field with kinetic Monte Carlo and finite element methods”, Bachelor’s thesis, 2016

[6] Kristjan Eimre, Stefan Parviainen, Alvo Aabloo, Flyura Djurabekova, Vahur Zadin, “Application of the general thermal field model to simulate the behaviour of nanoscale Cu field emitters “, Journal Of Applied Physics **118**, 033303, 2015

[7] G. A. Izquierdo, SEM analysis of HDS accelerating structures from recent 30 GHz tests at CTF3, in: Proceedings of the CLIC Meeting, 2007, http:// clic-meeting.web.cern.ch/clic-meeting/2007/01_12ga.pdf

[8] E. Baibuz, R. Aare *et al.*, “Growth mechanism of a nano-protrusion on a tungsten tip under electric field”, MeVArc 2017, https://indico.cern.ch/event/521667/contributions/2409295/attachments/1432931/2203912/mevarc_ekaterina_2017-final.pdf

[9] H. Yanagisawa *et al.*, “Laser-induced asymmetric faceting and growth of nano-protrusion on a tungsten tip”, APL Photonics **1**, 091305, 2016

[10] Nagaoka, K.; Fujii, H.; Matsuda, K.; Komaki, M.; Murata, Y.; Oshima, C.; Sakurai, T.: App. Surf. Sci. **182**, 12, 2001

[11] Fu, T-Y.; Cheng, L-C.; Nien, C-H.; Tsong, T. T.: Phys. Rev. B 2001, **64**, 113401.

[12] L. van Someren *et al.*, “Work function measurements on macroscopic tungsten specimens”, Surface Science **20**, 221-234, 1970

[13] G. A. Mesyats, “Pulsed power”, 29-53, 2005

[14] S. Fujita, H. Shimoyama, “Mechanism of surface-tension reduction by electric-field application: Shape changes in single-crystal field emitters under thermal-field treatment“, Phys. Rev. B 2007, **75**, 235431.

[15] V. T. Binh, “*In situ* fabrication and regeneration of microtips for scanning tunnelling microscopy”, J. Microsc. **152**, 355, 1988

[16] P. Bettler, F. Charbonnier, “Activation Energy for the Surface Migration of Tungsten in the Presence of a High-Electric Field”, Phys. Rev. **119**, 85, 1960

[17] Kealhofer, C.; Foreman, S. M.; Gerlich, S.; Kasevich, M. A.: Phys. Rev. B, **86**,

035405, 2012

[18] COMSOL MultiPhysics 5.3 Reference Manual, 2017

[19] D. Halliday, R. Resnick, J. Walker, Fundamentals of Physics. John Wiley & Sons, 9th ed.,

2013.

[20] K. M. Rabe, C. H. Ahn, J. Triscone, “Physics of ferroelectrics – A modern perspective”, Springer, 2007

[21] COMSOL MultiPhysics 4.4 Reference Manual, 2013

[22] D. Morin, “Chapter 8: Electromagnetic waves”, lecture notes at Harvard University, www.people.fas.harvard.edu/~djmorin/waves/electromagnetic.pdf

[23] C. G. Someda, “Electromagnetic waves”, CRC Press, 2006

[24] W. D. Kimura, “Electromagnetic Waves and Lasers”, Morgan and Claypool Publishers, 2017

[25] J. G. van Badel, “Electromagnetic fields”, IEEE Press, 2007

[26] T. Örd, “Kondensaine teooria 2: Optilised, elektrilised ja magnetilised omadused”, lecture notes, Tartu University, 2016

[27] N. W. Ashcroft, D. Mermin, “Solid state physics”, Brooks Cole, 1976

[28] M. A. Ordal *et al.*, “Optical properties of Al, Fe, Ti, Ta, W, and Mo at submillimeter wavelengths”, Applied Optics **27**, 1988

[29] L. Landau, E. M. Lifshitz, “Electrodynamics of continous media”, Pergamon Press, 1984

[30] C. P. Neo *et al.*, “Calculation of complex permeability of magnetic composite materials using ferromagnetic resonance model”, Journal of Applied Physics **107**, 083906, 2010

[31] S. Khakshouri, D. M. Duffy, “Influence of electronic effects on the surface erosion of tungsten”, Physical Review B **80**, 035415, 2009

[32] Z. Lin, L. Zhigilei, “Electron-phonon coupling and electron heat capacity of metals under conditions of strong electron-phonon nonequilibrium”, Physical Review B **77**, 075133, 2008

[33] W. L. McMillan, “Transition temperature of Strong-Coupled Superconductors, Phys. Rev. **167**, 331, 1968

[34] R. G. Forbes, “Simple good approximations for the special elliptic functions in standard Fowler-Nordheim tunneling theory for a Schottky-Nordheim barrier”, Applied physics letters **89**, 113122, 2006

[35] K. L. Jensen, “General formulation of thermal, field, and photoinduced electron emission”, Journal of Applied Physics **102**, 024911, 2007

[36] M. E. Kiziroglou, X. Li, A. A. Zhukov, P. A. J. De Groot, and C. H. De Groot, “Thermionic field emission at electrodeposited Ni–Si Schottky barriers”, Solid-State Electronics **52**, 1032–1038 2008

[37] E. W. Plummer, J. W. Gadzuk, “Surface states on Tungsten”, Phys. Rev. Letters **25**, 1970

[38] G. A. Haas, R. E. Thomas, “Distribution of Crystal Orientation and Work Function in Tungsten Ribbons”, Journal of Applied Physics **40**, 3919, 1969

[39] V. Zadin *et al.*, “Simulations of surface stress effects in nanoscale single crystals”, Modelling and Simulation in Materials Science and Engineering **26**, 2018

[40] K. Eimre, “Multiscale electrical and thermal simulations of metal surface defects in high electric field”, Master’s thesis, 2017

[41] R. G. Forbes, “Exact analysis of surface field reduction due to field-emitted vacuum space charge, in parallel-plane geometry, using simple dimensionless equations”, Journal of Applied Physics **104**, 084303, 2008

[42] J. P. Barbour *et al.*, “Space charge effects in Field Emission”, Physical Review **92**, 1953

[43] D.J. Griffiths, Introduction to Electrodynamics, 3rd edition, Addison Wesley, Upper Saddle River, N.J, 1999

[44] A.F. Bower, Applied Mechanics of Solids, CRC Press, 2009.

[45] COMSOL MultiPhysics 5.3 Structural Mechanics Module User’s Guide, 2017

[46] J. Kirs, G. Arjassov, “Sissejuhatus Lõplike Elementide Meetodisse I”, TTÜ kirjastus, 1999

[47] O. C. Zienkiewicz, R. L. Taylor, “The Finite Element Method”, Butterworth-Heinemann, 2000

[48] V. Jansson, E. Baibuz, F. Djurabekova, “Long-term stability of Cu surface nanotips”, Nanotechnology **27** 265708, 2016

[49] E. Baibuz *et al.*, “Migration barriers for surface diffusion on a rigid lattice: challenges and solutions”, arXiv preprint: arXiv:1707.05765, 2017

[50] V. Jansson *et al.*, “Surface diffusion in high electric fields”, Mini-MeVArc 2017 conference presentation https://indico.cern.ch/event/659586/contributions/2749113/attachments/1562635/2460908/jansson2017MiniMeVArc.pdf

[51] LAMMPS homepage, http://lammps.sandia.gov/doc/Section_intro.html

[52] M-C Marinica *et al.*, “Interatomic potentials for modelling radiation defects and dislocations in tungsten”, Journal of Physics: Condensed Matter **25**, 39, 2013

[53] M. Kazhdan, H. Hoppe, “Screened Poisson Surface Reconstruction”, ACM Transactions on Graphics **32**, 2013

[54] Properties of solid tungsten, Ho *et al*, COMSOL MultiPhysics 5.3 Material Database, 2017

[55] C. Y. Ho, R. E. Taylor, “Thermal expansion of solids”, ASM international, 1998

[56] H. Yanagisawa, personal contact

[57] A. Kyritsakis *et al.*, “A general computational method for electron emission and thermal effects in field emitting nanotips”, Computational Materials Science **128**, 2017

[58] R. Trebino, “Frequency-Resolved Optical Gating: the Measurement of Ultrashort Laser Pulses”, Springer US, 2000

[59] H. Karik, K. Truus, “Elementide Keemia”, Kirjastus Ilo, 2003

[60] G. P. Škoro *et al.*, “Yield strength of molybdenum, tantalum and tungsten at high strain rates and very high temperatures”, Journal of Nuclear Materials **426**, 2012

[61] M. Cherkaoui, L. Capolungo, “Atomistic and Continuum Modeling of Nanocrystalline Materials”, Springer US, 2009

[62] K. Kuppart, “Nanocrystalline copper simulations in high electric fields”, Bachelor’s thesis, University of Tartu, 2015

[63] J. Zha *et al.*, “Enhanced THz guiding properties of curved two-wire lines”, Optical Society of America **24**, 2016

Appendices

Appendix A: Derivation of the electromagnetic Helmholtz wave equation

In the absence of charges, the Maxwell equations can be written in the following form [19,22]:

$$\nabla \times \boldsymbol{B} = \mu_0 \epsilon_0 \frac{\partial \boldsymbol{E}}{\partial t} \tag{89}$$

$$\nabla \times \boldsymbol{E} = -\frac{\partial \boldsymbol{B}}{\partial t} \tag{90}$$

$$\nabla \cdot \boldsymbol{D} = 0 \tag{91}$$

$$\nabla \cdot \boldsymbol{B} = 0 \tag{92}$$

Here, Ampere-Maxwell's law has been combined with equations 5-6, assuming vacuum environment. Upon taking the curl of Faraday's law, Ampere-Maxwell's law can be used in order to get the following [19,22]:

$$\begin{gathered} \nabla \times (\nabla \times \boldsymbol{E}) = -\nabla \times \frac{\partial \boldsymbol{B}}{\partial t} \\ \nabla \times (\nabla \times \boldsymbol{E}) = -\frac{\partial (\nabla \times \boldsymbol{B})}{\partial t} \\ \nabla \times (\nabla \times \boldsymbol{E}) = -\frac{\partial \left(\mu_0 \epsilon_0 \frac{\partial \boldsymbol{E}}{\partial t} \right)}{\partial t} \\ \nabla \times (\nabla \times \boldsymbol{E}) = -\mu_0 \epsilon_0 \frac{\partial^2 \boldsymbol{E}}{\partial t^2} \end{gathered} \tag{93}$$

The following vector identity can be used to simplify the left-hand-side of the derived equation [22]:

$$\boldsymbol{A} \times (\boldsymbol{B} \times \boldsymbol{C}) = \boldsymbol{B}(\boldsymbol{A} \cdot \boldsymbol{C}) - \boldsymbol{C}(\boldsymbol{A} \cdot \boldsymbol{B}) \tag{94}$$

After substituting it into equation 12, we can use equation 10 for further simplification, to derive Helmholtz' wave equation for electric fields [22-24]:

$$\begin{gathered} \nabla(\nabla \cdot \boldsymbol{E}) - (\nabla \cdot \nabla)\boldsymbol{E} = -\mu_0 \epsilon_0 \frac{\partial^2 \boldsymbol{E}}{\partial t^2} \\ \frac{1}{\mu_0 \epsilon_0} \nabla^2 \boldsymbol{E} = \frac{\partial^2 \boldsymbol{E}}{\partial t^2} \end{gathered} \tag{95}$$

The wave equation for magnetic fields can be derived analogously, by initially taking the curl from Ampere-Maxwell's law, yielding [22]:

$$\frac{1}{\mu_0 \epsilon_0} \nabla^2 \boldsymbol{B} = \frac{\partial^2 \boldsymbol{B}}{\partial t^2} \tag{96}$$

Appendix B: Derivation of the formalism of generalized electrical permittivity

Electrical current density $\boldsymbol{J}$ and the relation between $\boldsymbol{D}$ and $\boldsymbol{E}$ are defined, as follows [26]:

$$\begin{aligned} \boldsymbol{J} &= \sigma(\omega)\boldsymbol{E} \\ \boldsymbol{D} &= \epsilon_0 \epsilon(\omega)\boldsymbol{E} \end{aligned} \tag{97}$$

These can be combined with the Ampere-Maxwell law [26]:

$$\nabla \times \boldsymbol{H} = \boldsymbol{J} + \frac{\partial \boldsymbol{D}}{\partial t} = \left(\sigma(\omega) - i\omega\epsilon_0 \epsilon(\omega)\right)\boldsymbol{E} \tag{98}$$

Now, generalized complex permittivity can be introduced [26]:

$$\hat{\epsilon}(\omega) = \epsilon(\omega) + i\frac{\sigma(\omega)}{\epsilon_0 \omega} = 1 + \chi_e(\omega) + i\frac{\sigma(\omega)}{\epsilon_0 \omega} \tag{99}$$

This simplifies Ampere-Maxwell's law to the following form:

$$\nabla \times \boldsymbol{H} = \frac{\partial \boldsymbol{D}}{\partial t} = \frac{\partial\left(\epsilon_0 \hat{\epsilon}(\omega)\boldsymbol{E}\right)}{\partial t} \tag{100}$$

Gauss' law can also be simplified, using the equation of continuity [26]:

$$\frac{\partial \rho}{\partial t} + \nabla \cdot \boldsymbol{J} = 0 \tag{101}$$

Charge density ρ is given by Gauss' law:

$$\nabla \cdot \boldsymbol{D} = \rho \tag{102}$$

For a monochromatic electromagnetic wave, the general solution is [25-26]:

$$\boldsymbol{D}(t) = \boldsymbol{D_0} e^{-i\omega t} \tag{103}$$

Thus, the time derivative of the charge density:

$$\frac{\partial \rho}{\partial t} = \nabla \cdot \frac{\partial \boldsymbol{D}}{\partial t} = -i\omega \nabla \cdot \boldsymbol{D} = -i\omega\rho \tag{104}$$

The equation of continuity can be combined with this result, using additionally the given definition of current density [26]:

$$\rho = -\frac{i}{\omega}\nabla \cdot \boldsymbol{J} = -\nabla \cdot \left(i\frac{\sigma(\omega)}{\omega}\boldsymbol{E}\right) \tag{105}$$

Using Gauss' law again, for the left-hand side of the equation, gives the following result:

$$\epsilon_0 \epsilon(\omega) \nabla \cdot \boldsymbol{E} = -\nabla \cdot \left(i \frac{\sigma(\omega)}{\omega} \boldsymbol{E} \right) \tag{106}$$

Introducing the generalized form of complex permittivity to the above equation results in the following form of Gauss' law [26]:

$$\nabla \cdot \left(\epsilon_0 \hat{\epsilon}(\omega) \boldsymbol{E} \right) = \nabla \cdot \boldsymbol{D} = 0 \tag{107}$$

Incidentally, the other 2 Maxwell laws remain unchanged, when using the generalized formalism. Therefore, Maxwell's equations, modified for using the generalized electrical permittivity formalism, appear in the following form [26]:

$$\begin{gathered} \nabla \times \boldsymbol{E} = \frac{-\partial \boldsymbol{B}}{\partial t} \\ \nabla \cdot \boldsymbol{B} = 0 \\ \nabla \times \boldsymbol{H} = \frac{\partial \boldsymbol{D}}{\partial t} \\ \nabla \cdot \boldsymbol{D} = 0 \end{gathered} \tag{108}$$

Appendix C: Laser spectrum analysis

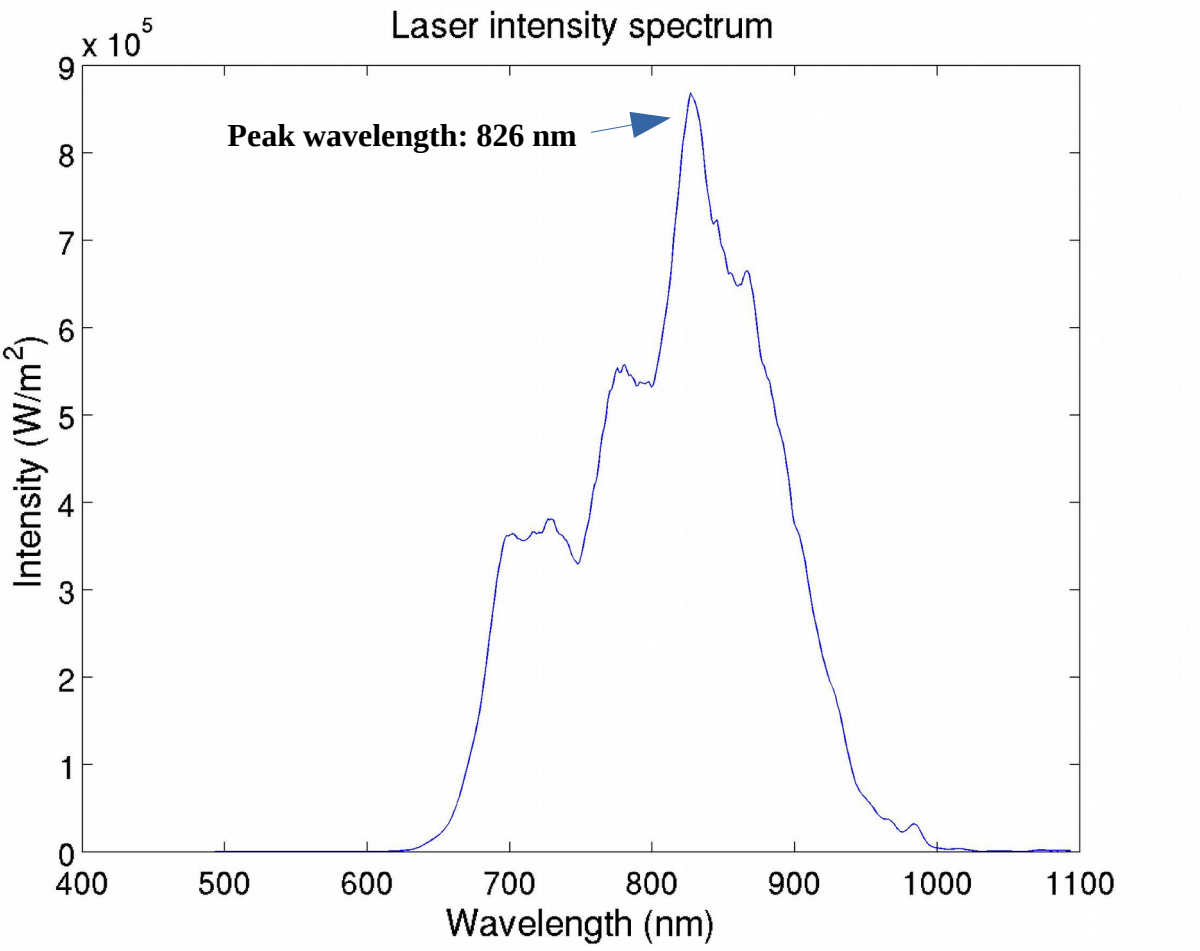

Illustration 29: Spectrum of the laser used in the experiment [56]

Intensity is defined, as follows [58]:

$$I = |E^2| \tag{109}$$

In the model, a plane wave at the peak intensity wavelength is used. To not artificially induce energy loss, the intensity spectrum is integrated over wavelengths, and the square root of the integral is set as the amplitude of the plane wave E_0 [58]:

$$E_0 = \sqrt{\int I \, d\lambda} \approx 9800 \, V/m \tag{110}$$

The following general relations allow transferring from wavelength dependence to frequency dependence [58]:

$$f = \frac{\omega}{2\pi} = \frac{c}{\lambda} \tag{111}$$

Here, f is frequency, ω is angular frequency, c is the speed of light, and λ is the wavelength. Using these relations, the peak angular frequency can be calculated: $\omega = 2.28\,PHz$.

Appendix D: Electronic conductivity and electron-phonon coupling factor

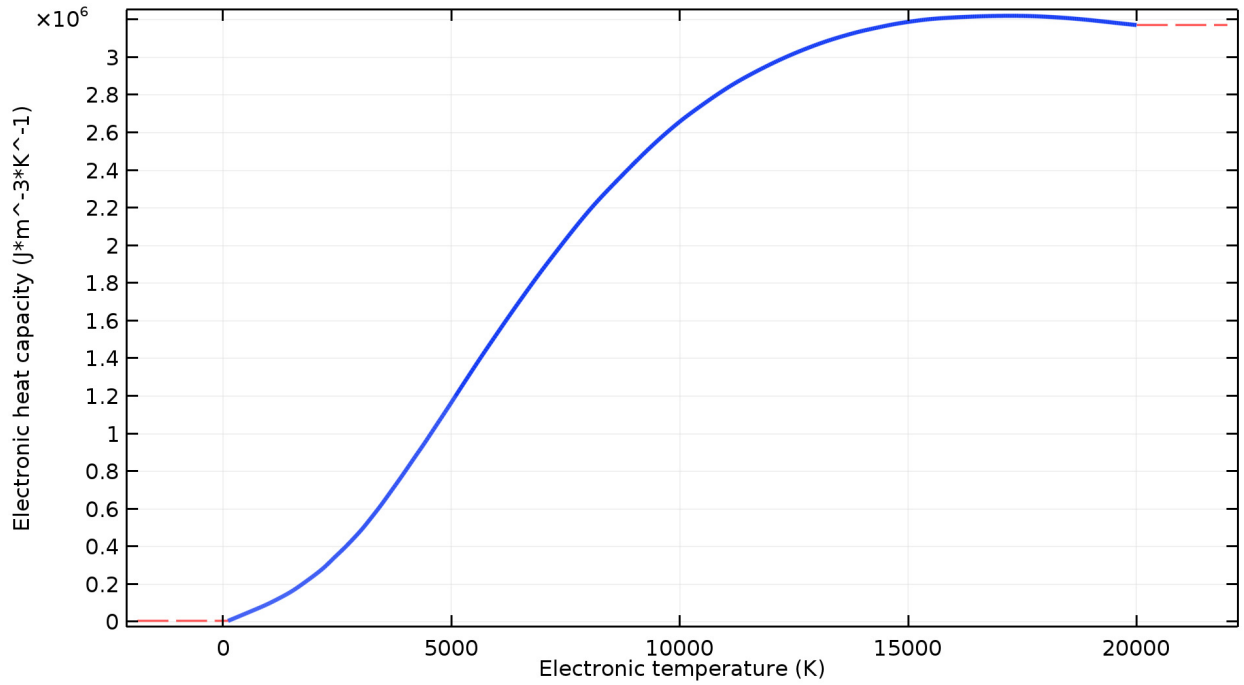

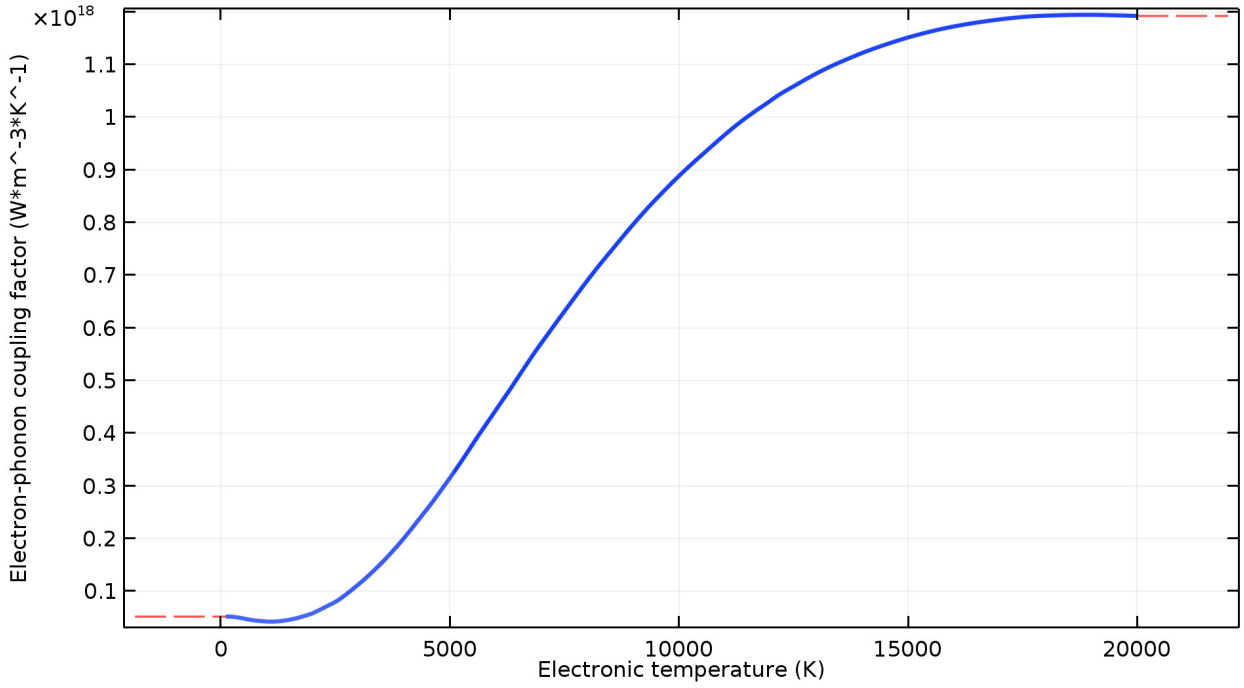

Illustration 30: Electronic heat capacity and electron-phonon coupling factor, assuming constant extrapolation (red) [32].

Appendix E: Skin depth estimation

Skin depth δ is the depth, at which the amplitude of the electromagnetic wave, that entered the crystal, has dropped to $1/e \approx 36.8\,\%$ of its incident amplitude. It can approximately be calculated with the following formula [63]:

$$\delta = \sqrt{\frac{2}{\omega \mu_0 \sigma}} \tag{112}$$

Here, $\mu_0 = 1.257 \cdot 10^{-6} \frac{m \cdot kg}{s^2 A^2}$ is the permeability of free space, σ is the electrical conductivity of the material, and ω is the angular frequency of the incident electromagnetic wave. With the electrical conductivity of the tungsten at 293 K being $\sigma = 1.86 \cdot 10^7 \frac{1}{\Omega m}$, and $\omega = 2.28 \cdot 10^{15} Hz$ the angular frequency of the electromagnetic wave used in this work, the skin depth of tungsten is **6.13 nm** [48].

Appendix F: Simulation geometries

Geometry for simulating thermal and mechanical behaviour

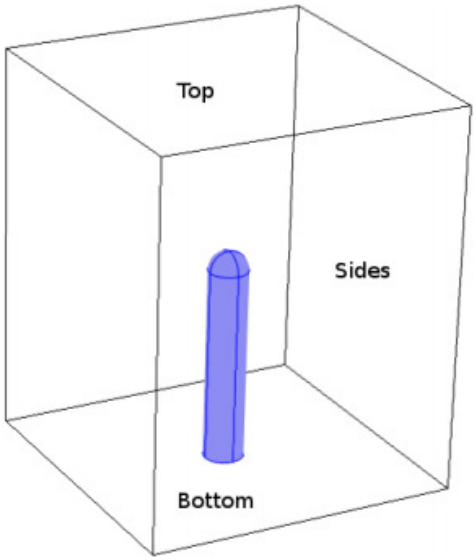

Illustration 31:

Simulation box height: 5000 nm

Simulation box width: 4000 nm

Simulation box depth: 4000 nm

Cylinder radius: 250 nm

Cylinder height: 2500 nm

Geometry for calculating emission patterns on surfaces extracted from molecular dynamics simulations

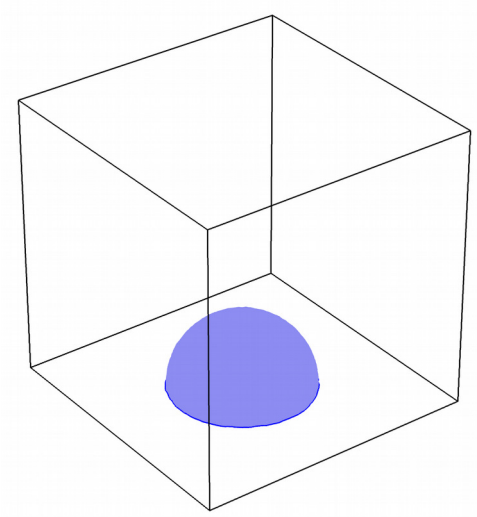

Illustration 32:

Simulation box height: 400 nm

Simulation box width: 400 nm

Simulation box depth: 400 nm

Approximate tip radius: 250 nm

Geometry for calculating emission patterns on surfaces extracted from Kimocs simulations

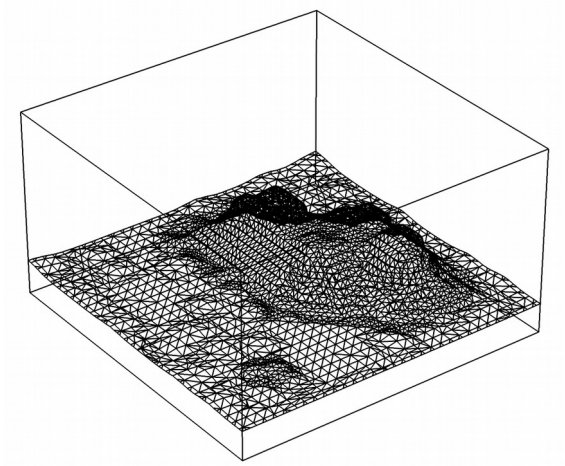

Illustration 33:

Simulation box height: 30 lattice constants

Simulation box width: 51 lattice constants

Simulation box depth: 51 lattice constants

Non-exclusive licence to reproduce thesis and make thesis public

I, Robert Aare,

1. herewith grant the University of Tartu a free permit (non-exclusive licence) to:

1.1. reproduce, for the purpose of preservation and making available to the public, including for addition to the DSpace digital archives until expiry of the term of validity of the copyright, and

1.2. make available to the public via the university's web environment, including via the DSpace digital archives, as of **31.05.2021** until expiry of the term of validity of the copyright,

“Modeling femtosecond-laser-induced faceting on tungsten surfaces, using the two temperature model”

supervised by Vahur Zadin

2. I am aware of the fact that the author retains these rights.

3. This is to certify that granting the non-exclusive licence does not infringe the intellectual property rights or rights arising from the Personal Data Protection Act.

Tartu**, 31.05.2018**